International Journal of Hydrogen Energy 116 (2025) 242–256

Contents lists available at ScienceDirect

International Journal of Hydrogen Energy

journal homepage: www.elsevier.com/locate/he

Heat integration and part-load performance of an SOEC-coupled Haber–Bosch process

Matthias Schiedeck [a,b,*], Rafael Nogueira Nakashima [a], Henrik Lund Frandsen [a]

[a] Technical University of Denmark, Department of Energy Conversion and Storage, Building 310, Fysikvej, Lyngby, DK-2800, Denmark
[b] Forschungszentrum Jülich GmbH, Institute for a Sustainable Hydrogen Economy (INW-4), Marie-Curie-Str. 5, 52428, Jülich, Germany

ARTICLE INFO

Dataset link: https://github.com/srnogueira/vivi

Keywords:
Green ammonia
Power-to-X
Haber–Bosch
Solid oxide electrolyzer (SOEC)
Heat integration
Part-load operation

ABSTRACT

Integrating the Haber–Bosch (HB) process with high-temperature water electrolysis for hydrogen production, such as using solid oxide electrolysis cells (SOEC), offers a promising opportunity to utilize the heat generated during ammonia synthesis for steam generation to partially cover the steam demand of the SOEC. While heat integration studies are typically conducted for full load conditions, this study explores the synergies between a thermoneutral, low-pressure SOEC system and a large-scale HB process across a load range from 10.7 % to 100 % by considering individual part-load strategies. At full load, optimal heat integration increases the efficiency of the SOEC system from 79.5 % to 93.0 % (LHV, DC). This results in an overall energy consumption of 26.4 GJ$t_{NH_3}^{-1}$ and a Power-to-Ammonia efficiency of 70.9 % (LHV, DC). During part-load operation, the specific energy consumption increases hyperbolically due to heat losses from the SOEC and kickback capacity control of the centrifugal make-up compressors in the HB process. Down to a part load of 32.4 %, the extra waste heat generated by the compressors replaces the electrical heating and hereby the total electricity consumption only increases moderately. At lower loads, however, the adopted part-load strategies lead to an increasingly steep rise in specific energy consumption. At the minimum load of 10.7 %, the specific energy consumption is 46 % higher than at full load.

1. Introduction

With specific CO_2 footprints of approximately 1.6 and 3.6 t_{CO_2} $t_{NH_3}^{-1}$ for methane- and coal-fired processes, respectively, the large share of industrial ammonia production in global CO_2 emissions amounts to approximately 1% to 2% [1,2]. This makes the production of ammonia the most CO_2-emitting process in the chemical industry [2]. As the cost of renewable power generation, especially from solar and wind energy, has fallen drastically over the last decade [3], electrification of the ammonia synthesis process (*Green ammonia, Power-to-Ammonia (PtA)*) is considered a promising approach for decarbonization [4]. At the same time, ammonia is increasingly being considered a suitable carrier molecule for international hydrogen transport [5]. Electrification can be achieved through the utilization of electrolyzers for hydrogen production, a concept that already accounted for approximately 30% of the global ammonia production capacity in the 1930s, mainly relying on hydro-power [6]. In contrast to hydropower, which is continuous but heavily tied to local availability, solar and wind energy are subject to fluctuations that place new challenges on the flexibility of production processes. The part-load capability and efficiency of individual process steps become a crucial factor for these systems.

Conventional Haber–Bosch (HB) plants based on natural gas are designed for steady-state operation with limited possibility and incentive for load flexibility [7]. Due to catalyst reactivation durations in the range of days [8,9], shutdowns and cold start-ups are avoided as far as possible and average to 5.7 per year [10]. Proposed strategies for load flexible operation are typically aimed at keeping the reactor temperature and pressure reasonably close to the design case, while varying or temporarily stopping production [11]. This is done in order to limit material fatigue [12], dangerous temperature increases with associated catalyst degradation [13] and similar effects. Suggestions commonly address loop pressure control by inert accumulation [13], reducing recycle compressor power [14], or using anti-surge/kickback valves [12,15]. Investigated temperature control strategies include increasing the coldshot [8] or changing the reactor inlet composition. For example, it is possible to reduce the H_2/N_2 ratio to decrease reactivity and shift the equilibrium to the reactant side [16]. Other approaches suggest to increase the ammonia concentration at the reactor inlet to

* Corresponding author at: Forschungszentrum Jülich GmbH, Institute for a Sustainable Hydrogen Economy (INW-4), Marie-Curie-Str. 5, 52428, Jülich, Germany.
E-mail address: m.schiedeck@fz-juelich.de (M. Schiedeck).

https://doi.org/10.1016/j.ijhydene.2025.02.335
Received 10 November 2024; Received in revised form 14 February 2025; Accepted 20 February 2025
Available online 12 March 2025
0360-3199/© 2025 The Authors. Published by Elsevier Ltd on behalf of Hydrogen Energy Publications LLC. This is an open access article under the CC BY license (http://creativecommons.org/licenses/by/4.0/).

limit conversion by means of a separator bypass or higher separator temperature [17]. Moreover, recent work has been reported on modified reactor designs [18] and control concepts [19,20] targeting load flexibility.

In addition to solutions for the HB process, large scale production of green ammonia will also require novel approaches for hydrogen production. For thermodynamic and kinetic reasons, high-temperature electrolysis, e.g. using solid oxide electrolysis cells (SOECs), features an inherently higher efficiency compared to low-temperature alternatives [21]. The advantage of SOECs as electrolysis technology can be further expanded by heat integration with an exothermic downstream reaction, e.g. ammonia synthesis in the HB process, to partially cover the steam demand of the SOEC [21]. The ability of SOECs to operate flexibly is crucial for adapting to fluctuations in the supply of renewable energy. Load flexible operation of individual electrolysis stacks is generally associated with the need for temperature control to reduce excessive temperature gradients and thermal stress within the cells [22]. Especially at non-thermoneutral operating points, possible operating strategies include electrical heating as well as cooling by varying the air flow rate [23]. Another proposed strategy for load-flexible operation is hot-idling individual stacks as needed. This enables maintaining the efficiency advantages of thermoneutral operation [21] of the remaining stacks under variable load [24]. In this context, operating strategies for hot-idling/stand-by operation [25] and minimizing associated heat losses, e.g. by using hot-boxes [26] play a major role.

Load-flexibility of SOECs and the HB process as individual technologies is essential for managing intermittent renewable energy supply. However, while the aforementioned heat integration between SOECs and the HB process offers substantial possibilities for energy efficiency improvement, the impact of load-flexible operation on this thermal synergy remains largely unexplored. One of the first and frequently cited works investigating the coupling of SOEC and the HB process was reported by Cinti et al. [27]. However, as pointed out by Dechany et al. [4] and Hansen [28], among other things, they overestimated the potential of heat integration by choosing the operating temperature of the ammonia reactor too high. Zhang et al. [29] investigated several green ammonia production processes including a PtA process using SOECs. As steam generation for the SOEC was found to be the limiting factor for system-level heat integration, their optimization resulted in maximizing heat generation within the system by increasing the operating pressure of the ammonia reactor to their upper bound of 200 bar and operating the SOEC exothermically with the maximum allowed temperature gradient of 120 °C. This resulted in a specific energy consumption of 24.76 GJ $t_{NH_3}^{-1}$. Campion et al. [30] considered, among other process configurations, a HB process (250 bar, 500 °C to 580 °C) coupled to SOECs operating near thermoneutral voltage at 750 °C. They considered heat integration by a single heat exchanger located downstream the external feed-effluent heat exchanger of the ammonia reactor and found a specific energy consumption of 28.78 GJ $t_{NH_3}^{-1}$. Nami et al. [31] investigated ammonia production routes employing alkaline and SOEC-based electrolysis and included current and future cost estimations. By coupling a HB process (200 bar) with low-pressure (1 bar) and high-pressure (30 bar) SOECs (thermoneutral operation at 750 °C), they found that 57% and 31%, respectively, of the steam demand could be satisfied by heat integration. This indicated an opposing effect between compression costs and level of heat integration on system efficiency, resulting in only slightly different overall specific energy consumptions of 26.64 GJ $t_{NH_3}^{-1}$ and 26.28 GJ $t_{NH_3}^{-1}$, respectively.

These studies on SOEC-based ammonia production typically either address heat integration at full-load operating conditions, or assume constant specific energy consumptions (and temperatures) in part-load operation, disregarding part-load efficiencies and nonlinearities. In addition, the impact of control strategies for SOEC systems, to operate in connection with renewables and downstream processes, into the system integration have not been evaluated in detail. Therefore, in this work, an SOEC-coupled HB process is investigated with respect to its load-dependent efficiency, considering particular part-load strategies for the two main technologies. In addition, optimal heat integration is ensured in order to identify energy integration potentials and describe their change depending on the load. Thus, this study aims to contribute to the development of efficient green ammonia systems by including the following novelties:

- A detailed model, simulation and analysis of an SOEC-coupled HB process, including a linear optimization of the energy integration potentials between the HB process, the SOEC system, and utilities.
- The simulation and analysis of part-load operation for the SOEC-coupled HB process, considering individual part-load strategies.
- A method to investigate the influence of non-linearities arising from part-load strategies on the potentials of energy integration.

Table 1
Overview of main modeling assumptions.

Technology τ	Included in heat integration	Part-load behavior	Details
SOEC system	Yes	Linear (except heat loss)	Section 2.1.1
Haber–Bosch process	Yes	Non-linear	Section 2.1.2
Air separation unit	No		
Refrigeration unit	Yes		
Steam boiler	Yes	Linear	Section 2.1.3
Cooling tower	Yes		
Electric heater	Yes		

2. Methods

The investigated system is shown in Fig. 1. It encompasses all considered sub-processes and utilities, which are collectively referred to as *technologies* in the remainder of this paper. Nitrogen is assumed to be provided by a cryogenic air separation unit (ASU). Hydrogen is produced from low-pressure steam using a high-temperature electrolysis system based on SOECs. The two reactants are fed to the HB process in the stoichiometric ratio of H_2/N_2 = 3/1. The available utilities comprise a cooling tower (CT), an electrical heater (EH), a refrigeration unit (RU) and a steam boiler (SB). The process is designed to produce 1356 tons of ammonia per day (TPD) at full load. Heat integration, colored red in Fig. 1, is carried out through linear energy integration optimization. To analyze the impact of part-load operation on the potentials of heat integration, the considered load range from 10.7% to 100% is discretized into steps. At each load step, the technologies are described as linearized models, consisting of incoming and outgoing mass flows, power demand or supply, and heat transfers (HT). Details on the individual HTs are given in the supplementary information.

The goal of this study and the methodology is to identify potential heat integration synergies between the two main processes, the HB process and the SOEC system, along a load trajectory. Therefore, several main modeling assumptions were made to simplify the analysis. These assumptions are summarized in Table 1 for the individual technologies in Fig. 1. For a more detailed description, the reader is referred to the respective section.

Since the analysis is limited to a single load trajectory, time-dependent effects, such as loss of catalytic activity or degradation phenomena, that depend on the extent of load-flexible operation over their lifetime, are not considered in this work. Furthermore, the load trajectory is not analyzed in terms of dynamic load changes but rather used to identify synergies based on the load status. Consequently, each discrete load step is treated as stationary. As in Nami et al. [31], values for efficiency and energy consumption presented in this work reflect only the process performance, assuming ideal electrical power conversion for all power-drawing equipment.

In the remainder of this section, the modeling approach of each technology and the method of energy integration optimization are explained in more detail.

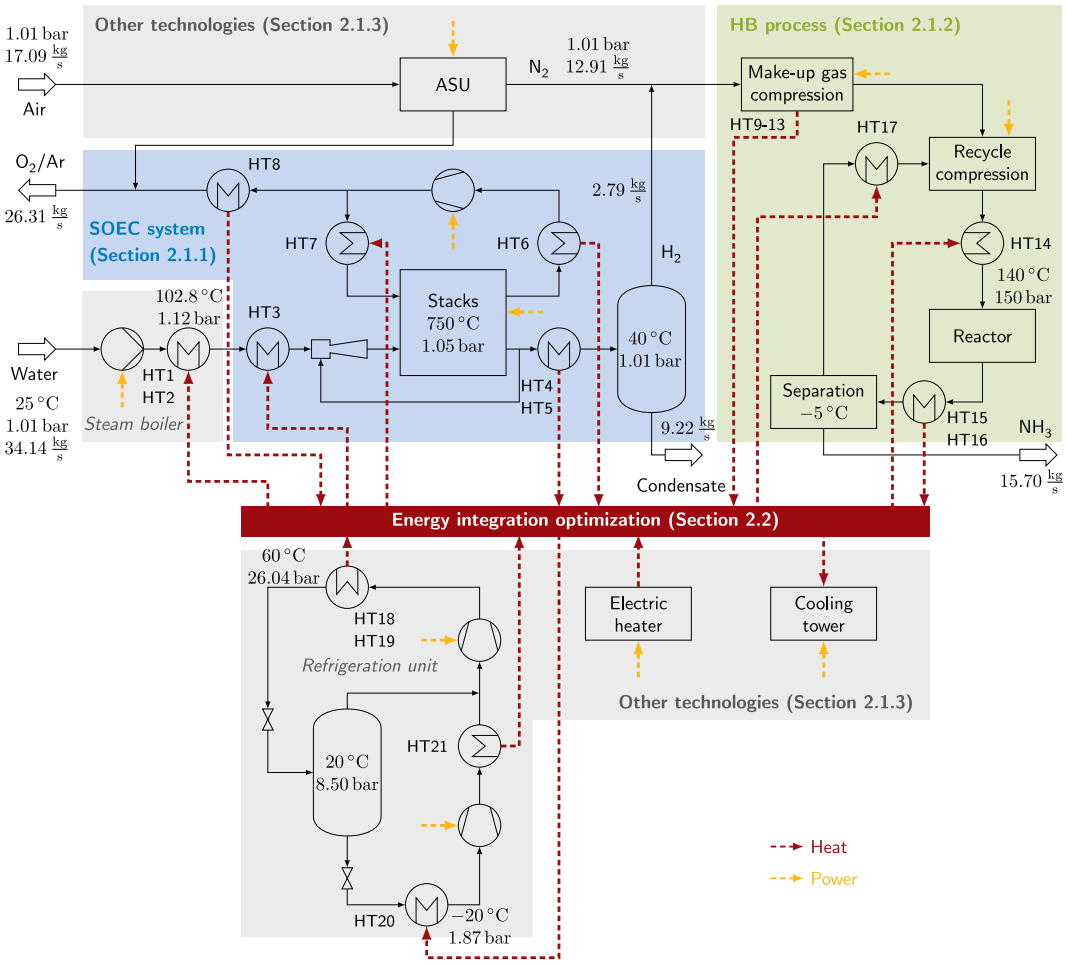

Fig. 1. Process flow diagram of the SOEC-coupled HB process. The red dashed lines indicate heating and cooling demands that are used for energy integration optimization. The yellow dashed lines indicate the power demand of the respective unit. Stream information correspond to full load operation. Details on the individual heat transfers (HT) are given in the supplementary information. (For interpretation of the references to color in this figure legend, the reader is referred to the web version of this article.)

2.1. Process modeling

In this subsection, the modeling of the individual technologies is addressed. The model of the SOEC and the HB process as well as their part-load strategies are discussed in detail.

2.1.1. SOEC system

Model description. For the solid oxide electrolysis system, the same model as presented in Nakashima et al. [32] is used. It is implemented in the Julia programming language. The system consists of the electrolysis stacks in whose cells the overall electrolysis reaction in Eq. (1) takes place. In addition, several Balance-of-Plant (BoP) components (heat exchangers, blower, ejector, separator) are included, as shown in Fig. 1.

$$H_2O \longrightarrow H_2 + 0.5\ O_2 \tag{1}$$

Saturated low-pressure steam (1.12 bar, 102.8 °C) is supplied to the system and then superheated to the operating temperature of 750 °C. To maintain reducing conditions and ensure an inlet hydrogen mole fraction of 10%, a portion of the cathode off-gas is recycled. The anode side is operated with oxygen instead of sweeping with air [33]. This design allows for oxygen as a by-product and thermal management of the stack [29]. Compared to an air sweep, it offers higher system efficiency by avoiding the need to heat the air flow from ambient temperature to the operating temperature of the SOEC [34]. However, it is important to note that handling hot pure oxygen requires safety measures in the form of material specifications and industrial protocols [35]. Water in the cathode off-gas is condensed and separated, yielding a pure H_2 product stream. The cells are assumed to operate at thermoneutral voltage, i.e. their heat demand is fully met by internal resistive heating (Joule heating). For the operating temperature of 750 °C, this corresponds to an operating cell voltage of $V_{op} = 1.285$ V. Table 2 summarizes the main assumptions of the system.

Table 2
Electrolysis system parameters.

Parameter	Value	Unit
Operating cell voltage (thermoneutral)	1.285	V
Stack inlet temperature	750	°C
Stack inlet pressure	1.05	bar
Minimum molar fraction H_2 at cathode inlet	0.1	–
Molar fraction O_2 at anode inlet	1.0	–
Fuel utilization efficiency	0.7	–
Pressure drop stack	0.04	bar
Pressure drop ejector	1.0	bar

The cell model is derived from a quasi-2D solid oxide fuel cell model [36,37] and modified for the electrolysis reaction [38]. The electrochemical model parameters are taken from Nami et al. [35] and are given in Tables 3 and 4. The characteristic relationship between current density j and operating cell voltage V_{op} (polarization curve) is described by the model equations in Eqs. (2) to (8). The operating voltage V_{op} depends on the reversible cell voltage V_{rev} and various loss mechanisms, see Eq. (2). The reversible cell voltage V_{rev} is calculated by the Nernst equation in Eq. (3). It consists of two terms: The first term

Table 3
Electrochemical model parameters [35,38].

Parameter	Value	Unit
B_{Ω}	$7.8247 \cdot 10^{11}$	S K m^{-2}
$E_{\mathrm{act},\Omega}$	$8.0022 \cdot 10^{4}$	J mol^{-1}
α_{H_2}	0.77251	–
γ_{H_2}	$8.99769 \cdot 10^{6}$	A K^{-1} m^{2}
a	−0.0538348	–
b	0.48814	–
E_{act,H_2}	$1.20051 \cdot 10^{5}$	J mol^{-1}
α_{O_2}	0.83035	–
γ_{O_2}	$2.43410 \cdot 10^{8}$	A K^{-1} m^{2}
m	0.18247	–
E_{act,O_2}	$1.48142 \cdot 10^{5}$	J mol^{-1}

Table 4
Electrolysis cell parameters [35,38].

Parameter	Value	Unit
Thickness cathode/anode/electrolyte	350/40/10	µm
Cathode/anode porosity	0.31/0.40	–
Cathode/anode tortuosity	2.52	–
Cathode/anode mean pore radius	1.75	µm
Cell dimensions	20 × 20	cm^2

contains the standard molar Gibbs free energy of reaction $\Delta\bar{G}^0_R\left(p^0,T\right)$, which depends only on temperature T. The second term contains a mixing term based on the partial pressures $p_{i,\mathrm{TPB}}$ of each species i at the triple phase boundary (TPB) between the electron conducting phase, the gas phase, and the oxide-ion conducting electrolyte. The number of electrons transferred is $z = 2$, while F and $\bar{R}$ denote the Faraday constant and the ideal gas constant, respectively. Losses from ohmic resistance R_{Ω} scale linearly with current density j and are modeled by a temperature-dependent Arrhenius approach in Eq. (4). The material-specific constant B_{Ω} and activation energy $E_{\mathrm{act},\Omega}$ are fitted model parameters, see Table 3. The activation overpotential $\eta_{\mathrm{act},\mathrm{H_2/O_2}}$ of each half-cell reaction is calculated using the Butler-Volmer equation in Eqs. (5) and (7). The catalytic activity of the electrodes is mainly depicted by the exchange current density $j_{0,\mathrm{H_2/O_2}}$. Its temperature dependence is modeled by an Arrhenius approach and partial pressure dependence is taken into account using power-law terms. The pre-factors $\gamma_{\mathrm{H_2/O_2}}$, power-law exponents a, b, and m, activation energies $E_{\mathrm{act},\mathrm{H_2/O_2}}$, and charge transfer coefficients $\alpha_{\mathrm{H_2/O_2}}$ are given in Table 3. Diffusion transport in the porous electrodes and its influence on the partial pressures $p_{i,\mathrm{TPB}}$ at the TPBs is included using the dusty-gas model (DGM) [39]. For the thermoneutral operating cell voltage $V_{\mathrm{op}} = 1.285\,\mathrm{V}$, the model results in an average current density of $-0.759\,\mathrm{A\,cm^{-2}}$.

$$V_{\mathrm{op}} = V_{\mathrm{rev}} - j\,R_{\Omega} - \eta_{\mathrm{act,H_2}} - \eta_{\mathrm{act,O_2}} \tag{2}$$

$$V_{\mathrm{rev}} = -\frac{\Delta\bar{G}^0_R\left(p^0,T\right)}{z\,F} + \frac{\bar{R}\,T}{z\,F}\,\ln\left(\frac{p_{\mathrm{H_2,TPB}}}{p_{\mathrm{H_2O,TPB}}}\cdot\left(\frac{p_{\mathrm{O_2,TPB}}}{p^0}\right)^{0.5}\right) \tag{3}$$

$$R_{\Omega} = \frac{T}{B_{\Omega}}\exp\left(\frac{E_{\mathrm{act},\Omega}}{\bar{R}\,T}\right) \tag{4}$$

$$j = j_{0,\mathrm{H_2}}\left(\exp\left(\frac{\alpha_{\mathrm{H_2}}\,z\,F\,\eta_{\mathrm{act,H_2}}}{\bar{R}\,T}\right) - \exp\left(-\frac{\left(1-\alpha_{\mathrm{H_2}}\right)\,z\,F\,\eta_{\mathrm{act,H_2}}}{\bar{R}\,T}\right)\right) \tag{5}$$

$$j_{0,\mathrm{H_2}} = \gamma_{\mathrm{H_2}}\,T\left(\frac{p_{\mathrm{H_2,TPB}}}{p^0}\right)^{a}\left(\frac{p_{\mathrm{H_2O,TPB}}}{p^0}\right)^{b}\exp\left(\frac{-E_{\mathrm{act,H_2}}}{\bar{R}\,T}\right) \tag{6}$$

$$j = j_{0,\mathrm{O_2}}\left(\exp\left(\frac{\alpha_{\mathrm{O_2}}\,z\,F\,\eta_{\mathrm{act,O_2}}}{\bar{R}\,T}\right) - \exp\left(-\frac{\left(1-\alpha_{\mathrm{O_2}}\right)\,z\,F\,\eta_{\mathrm{act,O_2}}}{\bar{R}\,T}\right)\right) \tag{7}$$

$$j_{0,\mathrm{O_2}} = \gamma_{\mathrm{O_2}}\,T\left(\frac{p_{\mathrm{O_2,TPB}}}{p^0}\right)^{m}\exp\left(\frac{-E_{\mathrm{act,O_2}}}{\bar{R}\,T}\right) \tag{8}$$

For more details on the SOEC system modeling assumptions and implementation, as well as the electrochemical model, the reader is referred to [35–38].

Part-load strategy. Due to the large-scale size of the ammonia production system, the electrolysis system is assumed to be constructed in a modular design consisting of many parallelly connected stacks. Although stack-level load following has been shown feasible [24,40] and was recently demonstrated in a long-term durability test [41], this work assumes that part load is realized by switching off individual stacks and keeping them on hot standby [21,42,43]. This allows the thermoneutral operating point to be maintained for the operating stacks regardless of the overall load. Moreover, it eliminates the need for additional stack temperature control strategies to avoid thermal stress. Therefore, quasi-linear behavior of the electrolysis stacks can be assumed. For simplicity, this also applies for the BoP components, whose part-load behavior (minimal volumetric flows, part-load efficiencies, heat transfer rating, etc.) is neglected. This assumption is discussed in Section 3.2.3. However, future work should consider their influence on the electrolysis system in more detail.

The cost of this modular part-load strategy is reflected in a constant, load-independent heat loss, which is assumed to be compensated by auxiliary electrical heating to keep the operating temperature constant. Its value is assumed to be 1% of the power demand of the SOEC system at full load. This loss is considered non-recoverable, i.e. it results from heat transfer through insulation to the environment or radiation from hot surfaces. Mathiesen et al. [44] give an estimate of 1% to 3% surface heat losses for mature >250 kW systems. In another study, a 40 kW SOEC system was found to have heat losses through the insulation of 3.1% [45]. It should be noted that the selected value of 1% is an estimate due to the lack of existing large-scale SOEC systems. However, it is reasonable to assume that the heat losses will be at the lower end of the values found in the literature due to size effects and optimized arrangement of high-temperature components for future large-scale plants. This assumption of load-independent heat loss is discussed in Section 3.2.3.

2.1.2. Haber–Bosch process

Model description. The HB process in Fig. 2 is modeled in Aspen HYSYS V11 with component properties and binary parameters taken from the HYSYS database. To account for non-ideal gas behavior, the Peng–Robinson equation of state is employed as a thermodynamic model. Assuming high-purity reactant generation, the make-up feed is considered inert-free [4].

The reactor design and its rating approach are adopted from Fahr et al. [46]. Similarly to Topsøe's S-300 reactor, it is composed of three adiabatic catalyst beds. Each bed is followed by a counter-current heat exchanger. All components are considered enclosed inside a pressure shell, following a cold-wall arrangement [47]. While the upper two heat exchangers enable indirect intercooling (IC) to maintain reasonable reaction rates, the lower internal feed-effluent heat exchanger (iFEHE) is used for heat recuperation. Varying the flow path of the reactor feed using three split factors (ξ_{Coldshot}, ξ_{IC} and ξ_{iFEHE}) enables strategies for temperature control and load reduction. The catalyst beds, in which the exothermic ammonia synthesis reaction in Eq. (9) takes place, are modeled as 1D pseudo-homogeneous plug flow reactors.

$$1.5\ \mathrm{H_2} + 0.5\ \mathrm{N_2} \rightleftharpoons \mathrm{NH_3} \tag{9}$$

The chemical reaction equilibrium in Eqs. (10) and (11) and kinetics in Eq. (12) are adopted from Fahr et al. [46]. The chemical equilibrium constant $K_f\left(T,p^0\right)$ follows the well-known model of Gillespie and Beattie [48]. It was refitted by Fahr et al. [46] to be compatible with the Peng–Robinson equation of state at a reference pressure of $p^0 = 1\,\mathrm{bar}$. The variables f, T, p, and y denote fugacity, temperature, pressure, and molar fractions, respectively.

$$K_f\left(T,p^0\right) = \prod_{i=1}^{K}\left(\frac{f_i\left(T,p,y_j\right)}{p^0}\right)^{\nu_i} \tag{10}$$

Table 5
Ammonia reactor design parameters.

	Fahr et al. [46]	This work	Unit
$V_{\text{Bed 1}}$	17.09		m^3
$V_{\text{Bed 2}}$	27.87		m^3
$V_{\text{Bed 3}}$	43.42		m^3
$UA_{\text{IC 1}}$	138.96		$kW\,K^{-1}$
$UA_{\text{IC 2}}$	63.31		$kW\,K^{-1}$
UA_{iFEHE}	146.44		$kW\,K^{-1}$
ξ_{Coldshot}	10.00	10.00	%
ξ_{IC}	80.10	81.08	%
ξ_{iFEHE}	9.90	8.92	%
$T^{\text{in}}_{\text{Bed 1}}$	357.4	356.6	°C
$T^{\text{out}}_{\text{Bed 1}}$	500.0	502.3	°C
$T^{\text{in}}_{\text{Bed 2}}$	393.1	393.8	°C
$T^{\text{out}}_{\text{Bed 2}}$	468.6	469.1	°C
$T^{\text{in}}_{\text{Bed 3}}$	384.0	384.3	°C
$T^{\text{out}}_{\text{Bed 3}}$	438.8	439.0	°C
$y^{\text{in}}_{NH_3,\text{Bed 1}}$	2.5	2.4	%
$y^{\text{in}}_{NH_3,\text{Bed 2}}$	11.6	11.6	%
$y^{\text{in}}_{NH_3,\text{Bed 3}}$	16.9	16.9	%
$y^{\text{out}}_{NH_3,\text{Bed 3}}$	21.0	21.0	%

$$= \exp\left(3.96301 + \frac{4554.63\,\text{K}}{T} - 2.31509\,\ln\left(\frac{T}{1\,\text{K}}\right)\right) \tag{11}$$

The reaction rate r_{NH_3} is based on the one by Dyson and Simon [49] and given as

$$r_{NH_3}\left(T,p,y_i\right) = k_0\,\exp\left(-\frac{E_A}{\bar{R}T}\right)\left[\left(K_f\left(T,p^0\right)\right)^2\,\frac{f_{N_2}\,f_{H_2}^{1.5}}{f_{NH_3}\left(p^0\right)^2} - \frac{f_{NH_3}}{f_{H_2}^{1.5}}\right]. \tag{12}$$

The pre-exponential factor $k_0 = 1.182\,979 \times 10^{15}\,\text{kmol bar}^{0.5}\,\text{h}^{-1}\,\text{m}^3_{\text{cat}}$ and activation energy $E_A = 168\,110.6\,\text{J mol}^{-1}$, which form the Arrhenius-Term, were adjusted by Fahr et al. [46] to again ensure compatibility with the Peng–Robinson equation of state. Catalyst particles are assumed to be small enough to neglect mass and heat transfer limitations. In industrial practice, e.g. in Topsøe's S-300 reactor, this is typically realized by a radial flow pattern to avoid excessive pressure drops [8]. Catalyst bed volumes $V_{\text{Bed i}}$ and UA values of the heat exchangers are adopted unchanged from Fahr et al. [46]. The split factors had to be slightly adjusted due to differences in the simulation environments, see Table 5. At full load, the reactor is operated at a design pressure of 150 bar. Pressure drops within the catalyst beds (0.6 bar at full load) and heat exchangers (0.3 bar at full load for each side), as well as their quadratic scaling as a function of the molar flow rate, are taken from Fahr et al. [46] without change. Heat transfer coefficients are treated analogously and are assumed to scale with an exponent of 0.7 as a function of molar flow [46].

The reactor effluent is cooled down to the separation temperature of −5 °C [46]. Concerning the subsequent linearization of the model, the cooling process is segmented into two steps. This was done due to the distinct change in heat capacity at the ammonia dew point. They are associated with a design pressure drop of 2.9 bar and 2.7 bar, respectively, again scaling quadratically with molar flow. In total, this aligns with the model of Fahr et al. [46]. To emulate multiple pressure-staged separation steps, the high-pressure flash separation is extended by a component split, which reintroduces the dissolved reactants back into the loop [46]. For the separation section, the Peng–Robinson–Stryjek–Vera (PRSV) modification is chosen in analogy to Fahr et al. [46].

Part-load strategy. The part-load strategy of the HB loop is based on the findings of Fahr et al. [46]. While they considered only the two outermost load cases, i.e. full and minimum load, this paper includes intermediate load states along a heuristic trajectory. Thus, the load-dependence of heat transfers and their temperature levels can be captured and subsequently used for heat integration optimization. This trajectory is divided into two subsequent stages. The first stage consists of a gradual reduction of pressure and volumetric flow down to their minimum values of 100 bar and 40% of the design volumetric flow, respectively, as specified by Fahr et al. [46]. Lowering the material stream through the reactor inevitably leads to an increase in residence time and, especially in the first catalyst bed, to a steeper adiabatic temperature rise. To avoid catalyst damage due to an excessively high temperature, the outlet temperature of the first catalyst bed $T_{\text{Bed 1,out}}$ must be kept at its design value. In the first stage, this is realized by means of the coldshot ξ_{Coldshot}. In the second stage, the pressure and volumetric flow have reached their minimum values and must not be reduced any further. As shown by Fahr et al. [46], even lower part load can be achieved by decreasing the fraction of reactor feed to the intercoolers. Thus, the reactor feed fraction ξ_{IC} is gradually decreased. The coldshot is kept constant. During this stage, the outlet temperature of the first catalyst bed $T_{\text{Bed 1,out}}$ is prevented from exceeding its design value by opening the separator bypass ξ_{Bypass}. This increases the ammonia fraction at the reactor inlet and slows down the reaction.

Due to the intended large-scale capacity of the plant and the associated flow rates, the compressors are assumed to be of centrifugal type aligning with industrial practice [8]. Each compressor is considered with a constant isentropic efficiency of 75% [50]. Following the approach of Dechany et al. [4], electrical drives are assumed instead of conventional steam turbines. Drive-related losses are considered negligible. The make-up gas compression is realized in $N = 5$ stages with intercooling, owing to the temperature increase upon compression. Assuming that the hot discharge of each compression stage is cooled down to its initial temperature at the suction side (40 °C), the ideal compression ratio Π of each stage is calculated by Eq. (13) [51]. Pressure losses in the intercoolers are neglected for simplification. The initial pressure of the fresh make-up gas from SOEC and ASU is denoted by p_{in} and the pressure after the last make-up compressor stage by p_{out}. For the considered operating pressure between 100 bar to 150 bar, this results in compression ratios between 2.50 and 2.72.

$$\Pi = \sqrt[N]{\frac{p_{\text{out}}}{p_{\text{in}}}} \tag{13}$$

The first choice of controlling compressor load is varying the rotational speed of the driver [52]. However, if the deviation from the nominal volumetric flow becomes too large, e.g. during start-up, shutdown, or part load, centrifugal compressors can experience aerodynamical instabilities (surge) which can lead to mechanical damage [8,52]. To avoid this, anti-surge control (kickback control) is typically implemented by recycling a part of the discharge gas back to the suction side of the compressor [8]. This paper adopts the approach of Sadlowski and van Beek [51] and assumes that the volumetric flow through the compressor can only be reduced to 65% of its nominal (full-load) value. For lower flow rates, the compressor must switch to kickback-operation to maintain the minimal volumetric flow. However, it is assumed that the isentropic efficiency remains invariable at 75% in part load as well. These assumptions for compressor capacity control are further discussed in Section 3.2.3.

Note that the load range is evaluated step-wise in stationary simulations and parameters are adjusted manually to ensure compliance with the boundaries for temperature and flow as described above. For future work, however, it is advisable to investigate the feasibility and responsiveness of this and other part-load strategies in dynamic simulations.

2.1.3. Other technologies

The other models briefly described in this paragraph comprise the air separation unit (ASU) and the utilities, as shown in Fig. 1. For those models, linear behavior is assumed over the entire load range without consideration of any part-load strategies.

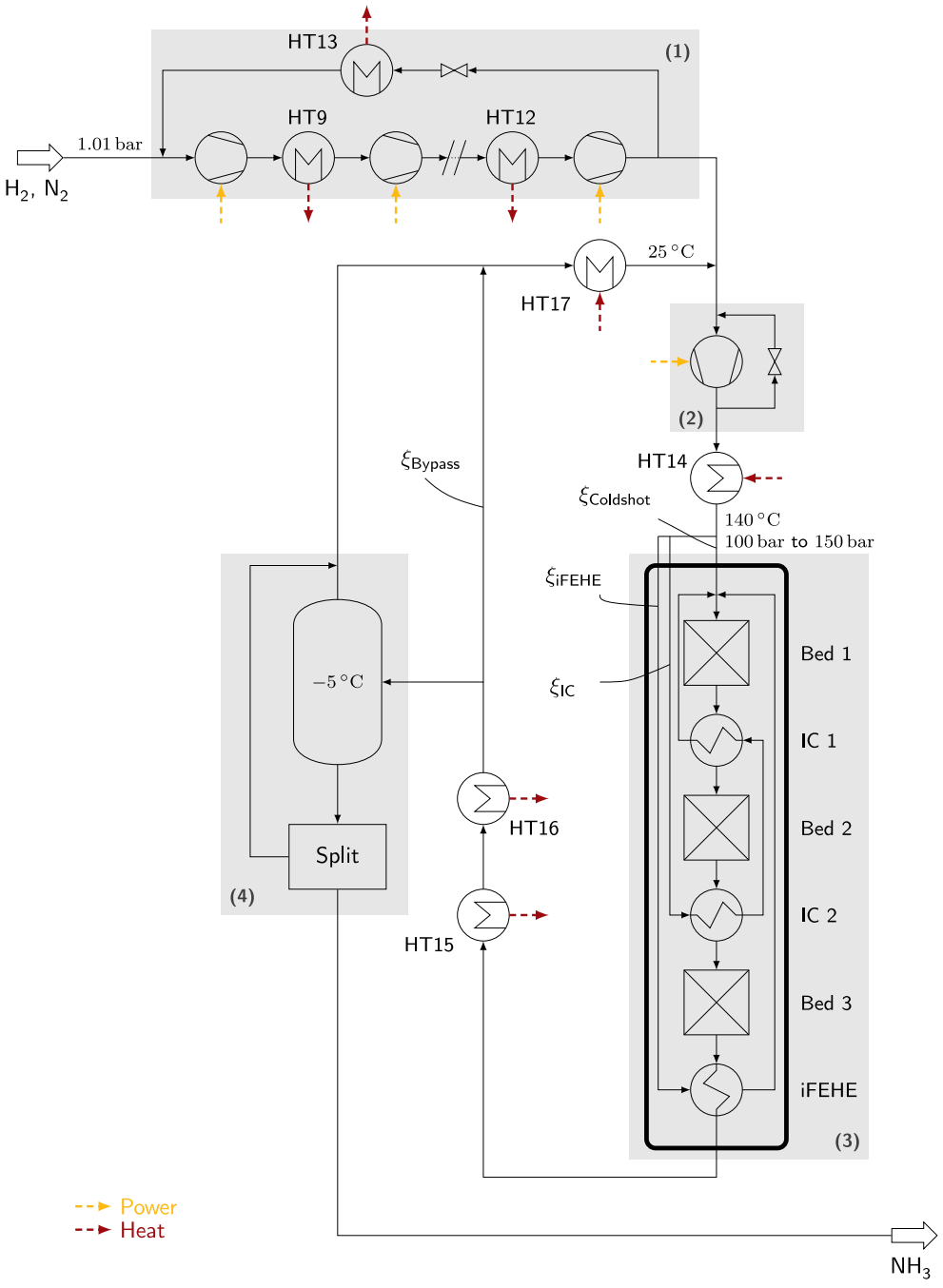

Fig. 2. Process flow diagram of synthesis gas compression and HB loop. (1) make-up gas compression, (2) recycle compression, (3) reactor, (4) separation. Reactor sketch adopted from [46]. Details on the individual heat transfers (HT) are given in the supplementary information.

The ASU is modeled as a black box with a constant specific energy consumption of 378 kJ $kg_{N_2}^{-1}$, corresponding to a cryogenic double-column process without integrated nitrogen compression [53]. It is assumed that argon is completely separated. This is assumed to result in a pure nitrogen product for the subsequent ammonia synthesis [4]. It is beyond the scope of this paper to consider the highly non-linear behavior of ASUs during load changes [54], the impacts on process equipment [55,56] and gas purity [57], and their complex process integration. Since neither the low-temperature refrigeration/distillation section nor the air purification/compression section of an ASU reaches temperatures above 100 °C [58,59], a condition required for low-pressure steam generation that could improve the efficiency of the SOEC, the ASU is excluded from the heat integration optimization for simplicity, as indicated in Fig. 1.

The layout of the refrigeration unit (RU) is based on Moshfeghian [60] and modeled in Aspen HYSYS. It incorporates two compression stages, each with an isentropic efficiency of 75%, and a flash economizer. Evaporation of the refrigerant R717 (pure NH_3) takes place at 1.87 bar and −20 °C. The saturated steam is then compressed and condensed at 26.04 bar and 60 °C. The saturated liquid is partially flash-evaporated at the intermediate pressure of 8.50 bar and separated in the flash economizer. This results in a temperature lift of 80 K and a COP of 2.015.

The steam boiler (SB) model is adopted from Nakashima et al. [38] and is located upstream of the SOEC. It is fed liquid water at 25 °C and ambient pressure and produces saturated steam at 1.12 bar (102.8 °C). The cooling tower (CT) acts as the final heat sink of the system. On the process side, a minimum temperature of 40 °C can be achieved in

counter-current flow. Its energy demand is adopted from Turton et al. [61]. The electric heater is assumed as an ideal heat source, i.e. the electrical power is fully converted into heat without any losses. Its temperature is set at 850 °C, similarly as proposed by Marechal and Kalitventzeff [62] for high temperature utility sources. This ensures that it can heat any stream within the considered system.

Note that technologies without mass-related inputs and outputs, i.e. refrigeration unit, electric heater and cooling tower (see lower part of Fig. 1) are available to the entire system as generic utilities. Inputs, outputs and heat transfers of all models at full load are given in the supplementary information.

2.2. Energy integration optimization

Optimal heat integration between the technologies is evaluated using the energy integration framework *Vivi* by Nakashima [63] based on the JuMP modeling language in Julia. The implemented linear programming optimization problem is given in Eqs. (15) to (20). Each technology $\tau \in \{\text{SOEC, ASU, HB, RU, SB, CT, EH}\}$ is represented as a linear system. To incorporate the non-linearities of the HB process arising from the employed part-load strategies, its load range is discretized into several steps. For each step, the HB process is considered linear and the energy integration optimization with the other technologies can thus be solved as a linear problem. In this way, the impact of part-load-related non-linearities on the potential of heat integration is investigated in a sequential manner.

The load of each step is characterized by a load factor LF, ranging from 10.7% to 100%. The load factor LF is defined in Eq. (14) as the ratio of the ammonia mass flow $\dot{M}_{\mathrm{NH_3,out}}$ leaving the production system at the current load state to the corresponding design value $\dot{M}^{\mathrm{Design}}_{\mathrm{NH_3,out}}$ at full load. Due to the assumption of inert-free reactants and thus omission of a purge stream, this definition also applies to the respective consumption of nitrogen and hydrogen.

$$\mathrm{LF} = \frac{\dot{M}_{\mathrm{NH_3,out}}}{\dot{M}^{\mathrm{Design}}_{\mathrm{NH_3,out}}} \tag{14}$$

For each load factor LF, the minimum total power demand $P_{\mathrm{el,tot}}$ is determined by optimization. The solver can linearly scale each technology, i.e. its power demand/supply P^{τ}_{el}, associated heat transfers $\dot{Q}^{\tau}_{n}$, and produced/consumed mass flows $\dot{M}^{\tau}_{i,\mathrm{prod/cons}}$, using multiplicative size factors γ^{τ} as decision variables. An exception is the HB process, whose non-linearities are modeled in Aspen HYSYS as described in Section 2.1 and linearized individually for each load factor as described above. For simplification, its power demand $P^{\mathrm{HB}}_{\mathrm{el}}$ and heat transfers $\dot{Q}^{\mathrm{HB}}_{n}$ with their corresponding source and target temperatures $T^{\mathrm{HB}}_{\mathrm{Source},n}$ and $T^{\mathrm{HB}}_{\mathrm{Target},n}$, respectively, are expressed as a function of the load factor LF in Eq. (20). Specific values of these relationships are given in Fig. 5 and in the supplementary information. Note that the optimization problem is solved sequentially for each load step characterized by the load factor LF. The load-independent, auxiliary heating $P^{\mathrm{SOEC}}_{\mathrm{el,auxiliary}}$ to compensate for the heat loss of the SOEC is considered separately in the objective function. The mass balance for each resource $i \in \{\mathrm{Air, Water, Steam, N_2, H_2, NH_3}\}$ is ensured by Eq. (16). Optimal heat integration is realized by enforcing the heat cascade constraint in Eq. (17), which is based on the work of Marechal and Kalitventzeff [62] and Papoulias and Grossmann [64]. Heat transfers involving phase changes (e.g. condensation or evaporation) are segmented into two steps due to the change in heat capacity. All heat transfers (HT) $\dot{Q}^{\tau}_{n}$ considered in the optimization are shown in Fig. 1. Each of them is divided into temperature intervals. The method used to determine these intervals (shifted temperatures) ensures a global minimum temperature difference of $\Delta T_{\mathrm{min}} = 15\,\mathrm{K}$ in the resulting heat network. The heat transfer of stream n of technology τ at the temperature interval k is denoted as $\dot{Q}^{\tau}_{n,k}$. The residual heat R_k of each temperature interval k is available to the solver as a decision variable. By constraining $R_k = 0$ at the two extremes of the cascade and $R_k \geq 0$ in between (ensuring heat exchange only from a higher to a lower temperature level) in Eq. (19), optimal heat integration is enforced using the available technologies. The reader is referred to the supplementary information (SI) for data of the linearized models used in the optimization and to [63] for more information on the optimization framework.

$$\min_{\gamma^{\tau},\,R_k} P_{\mathrm{el,tot}} = \sum_{\tau}^{N_{\tau}} P^{\tau}_{\mathrm{el}}\,\gamma^{\tau} + P^{\mathrm{SOEC}}_{\mathrm{el,auxiliary}} \tag{15}$$

subject to

$$\dot{M}_{i,\mathrm{in}} + \sum_{\tau}^{N_{\tau}} \gamma^{\tau}\left(\dot{M}^{\tau}_{i,\mathrm{prod}} - \dot{M}^{\tau}_{i,\mathrm{cons}}\right) = \dot{M}_{i,\mathrm{out}} \quad \forall i \tag{16}$$

$$R_{k-1} + \sum_{\tau}^{N_{\tau}} \gamma^{\tau}\left(\sum_{n}^{N} \dot{Q}^{\tau}_{n,k}\right) = R_k \quad \forall k \tag{17}$$

in which

$$\gamma^{\tau} \geq 0 \tag{18}$$

$$R_k \begin{cases} = 0 & \text{for} \quad k = 0, K \\ \geq 0 & \text{otherwise} \end{cases} \tag{19}$$

$$P^{\mathrm{HB}}_{\mathrm{el}},\ \dot{Q}^{\mathrm{HB}}_{n},\ T^{\mathrm{HB}}_{\mathrm{Source},n},\ T^{\mathrm{HB}}_{\mathrm{Target},n} = f\,(\mathrm{LF}) \tag{20}$$

(f is HB model in Aspen HYSYS)

2.3. Performance indicators

The performance of the system is assessed using the specific energy consumption in $\mathrm{GJ\,t^{-1}_{NH_3}}$ and the LHV-based efficiency. The specific energy consumption of each technology e^{τ} and the entire system e_{Sys} are related to the ammonia production at each load step and are calculated according to Eqs. (21) and (22), respectively.

$$e^{\tau} = \begin{cases} \dfrac{P^{\mathrm{SOEC}}_{\mathrm{el}} + P^{\mathrm{SOEC}}_{\mathrm{el,auxiliary}}}{\dot{M}_{\mathrm{NH_3,out}}} & \text{for } \tau = \mathrm{SOEC} \\ \dfrac{P^{\tau}_{\mathrm{el}}}{\dot{M}_{\mathrm{NH_3,out}}} & \text{else} \end{cases} \tag{21}$$

$$e_{\mathrm{Sys}} = \frac{P_{\mathrm{el,tot}}}{\dot{M}_{\mathrm{NH_3,out}}} \tag{22}$$

To determine the efficiency of the SOEC system, the energy content of the produced hydrogen, i.e. the product of hydrogen mass flow $\dot{M}^{\mathrm{SOEC}}_{\mathrm{H_2,prod}}$ produced by the SOEC and its lower heating value $\mathrm{LHV_{H_2}}$, is divided by the electrical energy input, see Eq. (23). The latter comprises the power demand $P^{\mathrm{SOEC}}_{\mathrm{el}}$ of the electrolysis, the auxiliary heating $P^{\mathrm{SOEC}}_{\mathrm{el,auxiliary}}$ to compensate for its heat loss, and the power demand $P^{\mathrm{EH}}_{\mathrm{el}}$ of the electrical heater. For the entire Power-to-Ammonia efficiency, the product of ammonia mass flow $\dot{M}_{\mathrm{NH_3,out}}$ and its lower heating value $\mathrm{LHV_{NH_3}}$ is set in relation to the total power demand $P_{\mathrm{el,tot}}$ of the system.

$$\eta_{\mathrm{SOEC}} = \frac{\dot{M}^{\mathrm{SOEC}}_{\mathrm{H_2,prod}}\,\mathrm{LHV_{H_2}}}{P^{\mathrm{SOEC}}_{\mathrm{el}} + P^{\mathrm{SOEC}}_{\mathrm{el,auxiliary}} + P^{\mathrm{EH}}_{\mathrm{el}}} \tag{23}$$

$$\eta_{\mathrm{Sys}} = \frac{\dot{M}_{\mathrm{NH_3,out}}\,\mathrm{LHV_{NH_3}}}{P_{\mathrm{el,tot}}} \tag{24}$$

3. Results and discussion

First, the results of full-load operation (LF = 100 %) for the SOEC-coupled HB process in Section 3.1 are presented and discussed. Then, in Section 3.2, the effects of the considered part-load strategies ($10.7\,\% \leq \mathrm{LF} \leq 100\,\%$) on heat integration and system performance are examined.

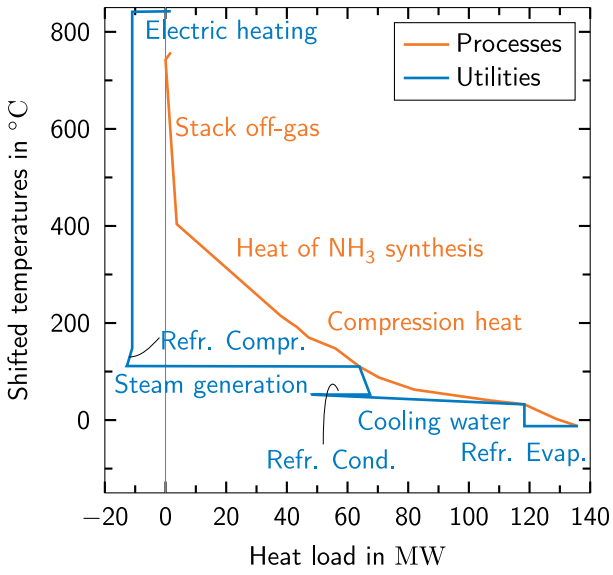

Fig. 3. Integrated composite curves of the overall system at full-load. Heat for low-pressure steam generation is provided by electric heater, stack off-gas, ammonia reactor effluent, and compressor waste heat.

Table 6
Specific energy consumption of technologies and the system.

Technology τ	P_{el}^{τ} in MW	e^{τ} in GJ $t_{NH_3}^{-1}$
SOEC system	343.5 + 3.4[a]	21.9 + 0.2[a]
Haber-Bosch process	38.5	2.5
Air separation unit	4.9	0.3
Refrigeration unit	8.8	0.6
Cooling tower	1.0	0.1
Electric heater	12.7	0.8
System	412.8	26.4

[a] Heat loss.

3.1. Full-load operation

The energy consumption of the individual technologies and the entire system at full load are given in Table 6. The SOEC system accounts for the largest share of total power demand at 84.1%, followed by the HB process at 9.3%. The make-up compressors dominate the energy demand of the HB process with 95.9%, which is due to the low inlet pressure of the reactants. It is shown that despite the optimal heat integration between the SOEC system and the HB process, there is still the need for electric heating in the system. Its overall value of 0.8 GJ $t_{NH_3}^{-1}$ is in good agreement with the estimate of Dechany et al. [4]. The energy demand of the ASU is relatively low, accounting for only 1.1% of the total energy requirement. Notably, its energy consumption is comparable in scale to the SOEC heat loss. For the entire Power-to-Ammonia (PtA) system, the optimization results in an energy demand of 26.4 GJ $t_{NH_3}^{-1}$. For a similar SOEC-based ammonia production system using an air separation unit, Hansen and Hendriksen [65] report a range of 25.9 GJ $t_{NH_3}^{-1}$ to 26.6 GJ $t_{NH_3}^{-1}$.

By optimally integrating the SOEC system with the HB process, the efficiency (LHV, DC) of the SOEC system in isolation can be increased from 79.5% to 93.0%. For the entire PtA system, this results in an efficiency (LHV, DC) of 70.9%. The integrated composite curves in Fig. 3 visualize the heat integration of utilities (cooling tower, electric heater, refrigeration unit and steam boiler) with regard to the processes (SOEC system, HB process). Integration with the HB process allows the heat from the ammonia synthesis reaction available in the reactor effluent and to a considerable extent the waste heat from the make-up and refrigeration compressors to be used for low-pressure steam generation. In the SOEC system, some heat from the stack off-gas is also used for steam generation. However, due to the high temperature of the off-gas, the majority of this heat is recuperated for steam overheating. The low heat capacity of the gases is reflected in the steep gradient in Fig. 3. All contributions reduce the need for electrical heating and thus increase the overall system efficiency. Nevertheless, 14.3% of the heat needed for steam generation, equivalent to 0.7 GJ $t_{NH_3}^{-1}$, still relies on electrical heating. This value also represents the theoretical potential for further efficiency improvement, if additional heat sources at suitable temperature for steam generation were introduced in the system. The remaining heat of 0.1 GJ $t_{NH_3}^{-1}$ supplied by the electrical heater is used for final steam superheating and O_2 reheating to reach the operating temperature of the SOEC. Heat below the threshold temperature for steam generation (including the 15 K minimum temperature difference) is dissipated by cooling water down to a process temperature of 40 °C. For lower temperatures, the refrigeration unit is used. Its condensation heat cannot be removed below 60 °C to maintain the temperature difference of 15 K to the cooling water heat sink (45 °C maximum temperature in counter flow on utility side).

An additional heat source at high temperatures would come from the exothermic operation of the SOEC at high current densities, as reported by Zhang et al. [29]. This strategy of using internal heat generation to reduce the external heating demand may, however, be limited. On the one hand, the temperature gradient caused by exothermal operation can impact the mechanical stability and ultimately the lifetime of the stacks [66]. The temperature difference of 120 °C reported by Zhang et al. [29] is based on an active cell area of 80 cm^2 [67], which exceeds the frequently considered rule-of-thumb-limit of 10 K cm^{-1} [34], beyond which cell damage can occur. On the other hand, operation at such high current density (−0.96 A cm^{-2}) reported by Zhang et al. [29] increases degradation and shortens the stack lifetime as well [68]. In addition, Hansen [69] and Beyrami et al. [70] note that if the temperature rises too much, raising the inlet temperature would no longer be available as a strategy to counter degradation. Exothermal operation of the SOEC to further reduce the external heating demand thus entails an economic tradeoff between the cost and frequency of stack replacement, and potential system integration benefits. From this perspective, lower-cost stacks may tolerate higher temperature gradients, generating more internal heat and reducing external heating requirements, while expensive stacks may require stricter thermal management to extend their operational lifetime.

3.2. Part-load operation

3.2.1. Part-load strategy of HB loop

The results of the part-load strategy for the HB loop are reported in Fig. 4. In the first stage (1), the material stream through the loop is reduced by decreasing pressure and volumetric flow to their minimum values of 100 bar and 40% of the design value, respectively [46]. This is shown in Fig. 4(a). The coldshot split $\xi_{Coldshot}$ is first increased for temperature control during this stage, see Fig. 4(b). Since the pressure reduction slows down the reaction as well, the coldshot can be reduced again at approximately LF = 50 %. To ensure controllability at every operating point, a minimum of $\xi_{Coldshot}$ = 10 % in analogy to [46] is maintained. At the end of the first stage (1), a load factor of LF = 24.7 % is reached.

In the second stage (2), the feed split ξ_{IC} to the intercoolers (ICs) is decreased, while pressure and volumetric flow are kept constant, see Figs. 4(a) and 4(b). Due to the autothermal characteristics and the oversized internal feed-effluent heat exchanger (iFEHE), this measure further reduces the ammonia production in the reactor. At the beginning of stage (2), the increase of heat recovery in the iFEHE outweighs the decrease in the ICs. The resulting temperature increase at the inlet of the first catalyst bed is counteracted by opening the separator bypass ξ_{Bypass} and thus increasing the ammonia concentration at the reactor inlet, see Fig. 4(b). It should be noted, that this measure mainly impacts

the temperature level in the first catalyst bed. As shown by [46], it does not have a significant effect on the load, i.e. the ammonia production, since the operating points of the catalyst beds just shift to higher ammonia fractions. Eventually, heat recuperation by the ICs is reduced to a level where the separator bypass can be closed again. At the end of the second stage (2), the minimum load factor of LF = 10.7 % is reached when intercooling is completely turned off. The difference to Fahr et al. [46], who report a minimum load of 13.1%, can mainly be attributed to the high sensitivity of heat transfer in the iFEHE and differences in the simulation environments. For example, slight differences in vapor–liquid equilibrium in the separator lead to a higher inlet temperature of the first catalyst bed at minimum load in our work.

The heat transfers $\dot{Q}_n^{\mathrm{HB}}$ of the HB process requiring cooling and their source temperatures, i.e. the heat potentially available for steam generation, are shown in Fig. 5 as a function of the load factor LF. For most of the load range, the reactor effluent is the largest heat source being available at 390 °C to 410 °C in stage (1). In stage (2), its temperature drops sharply down to approximately 245 °C as the heat recuperation is increasingly shifted towards the iFEHE. For pressurized operation of the SOEC, the considered part-load strategy of decreasing intercooling in the reactor thus may pose a limitation on heat integration. However, for the low-pressure SOEC assumed in this work, the reduction in reactor effluent temperature does not result in an additional reduction in heat integration potential. The reason for this will be discussed in Section 3.2.2.

Since the make-up feed supply linearly correlates with the load factor, the make-up compressors switch to kickback operation at LF = 65 % for the chosen capacity control method. As a result, for LF ≤ 65 %, not only the energy demand of the compressors becomes constant, but also their waste heat production. This is shown in Fig. 5(a). At the same time, heat removal in the kickback cooler increases proportional to compressor-internal recycling. Both compressor-related heat sources are available at a temperature of approximately 178 °C and can therefore be partially used for steam generation.

To illustrate the flow routing in the part-load strategy described above, Fig. 6 shows the three major part-load sections (subfigures a) and b) correspond to stage (1), while subfigure c) corresponds to stage (2)) in the process flow diagram. The streams are color-coded based on their temperature ranges within each part-load section. The split factors used for temperature control are emphasized in bold.

3.2.2. Performance of the PtA system

Fig. 7 shows the individual contribution of each technology to the total specific energy consumption of the PtA system. It should be kept in mind that these results obtained from the optimization in Eqs. (15) to (20) do not show a single system under different load conditions. Instead, they show the maximum theoretical potential for heat integration at each load factor LF.

SOEC heat loss. The SOEC system accounts for the dominant share of the total energy consumption owing to the high intrinsic energy demand of the electrolysis reaction. Due to the modular part-load strategy and the assumption of linear behavior of the BoP components, its contribution appears almost constant over a wide load range. For the discussion of these results, the reader is referred to Section 3.2.3. However, the load-independent, auxiliary heating to compensate for the heat loss of the SOEC causes the specific energy consumption to slowly increase hyperbolically as the load factor decreases. At full load (LF = 100 %), the heat loss of the SOEC alone is approximately 0.8% of the total power consumption. At LF = 24.7 % it already accounts for 3.0% and increases to 5.3% at minimum load (LF = 10.7 %), making it the third largest energy consumer in the PtA system. The SOEC heat loss is further discussed in Section 3.2.3.

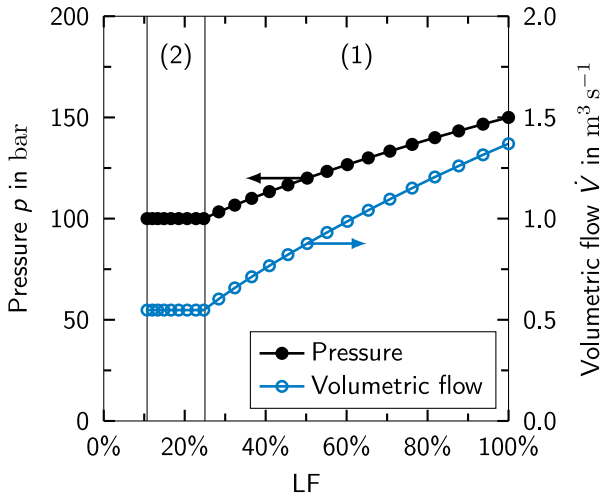

(a) Loop pressure and volumetric flow as a function of the load factor.

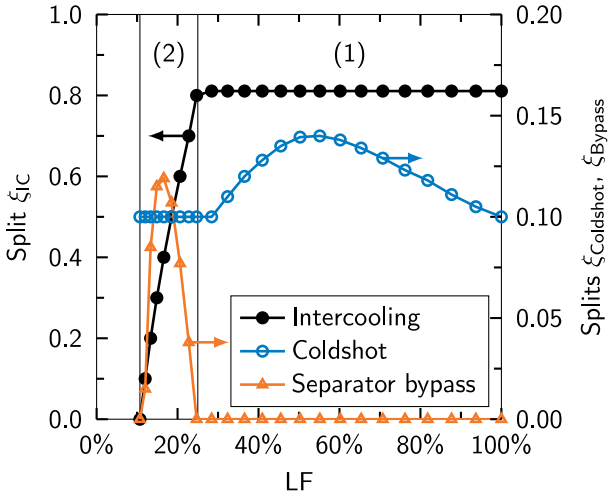

(b) Variation of available split factors for temperature control and load reduction.

Fig. 4. Part-load strategy of the HB process and measures for temperature control. (1) Reducing material stream, (2) Reducing intercooling.

Kickback operation of compressors. The energy consumption of the HB process consisting almost entirely of the energy demand of the make-up compressor, represents the second largest contribution to the total power demand. Initially, it decreases slightly from 9.3% at full load to 8.9% at LF = 65 % due to the gradual pressure reduction in stage (1) of the HB process part-load strategy. Below LF = 65 %, the compressor switches to kickback operation and starts internal recycling. This is reflected in a pronounced hyperbolic increase in specific energy consumption and can be observed in Fig. 7. At LF = 24.7 %, the fraction of the HB process rises to 19.3% and continues to shoot up to 34.4% at the minimum load (LF = 10.7 %). Owing to the quadratic scaling of pressure drops with molar flow, the power required by the recycle compressor becomes increasingly negligible at lower loads compared to the high power demand of the make-up compressor. However, as discussed before and shown in Fig. 5, kickback operation not only results in constant energy consumption of the make-up compressor, but also proportional waste heat generation. This additional heat is available for steam production and gradually replaces the electric heater down to a load factor of LF = 32.4 %. In the medium load range, this creates an interesting synergy between the SOEC system and the HB

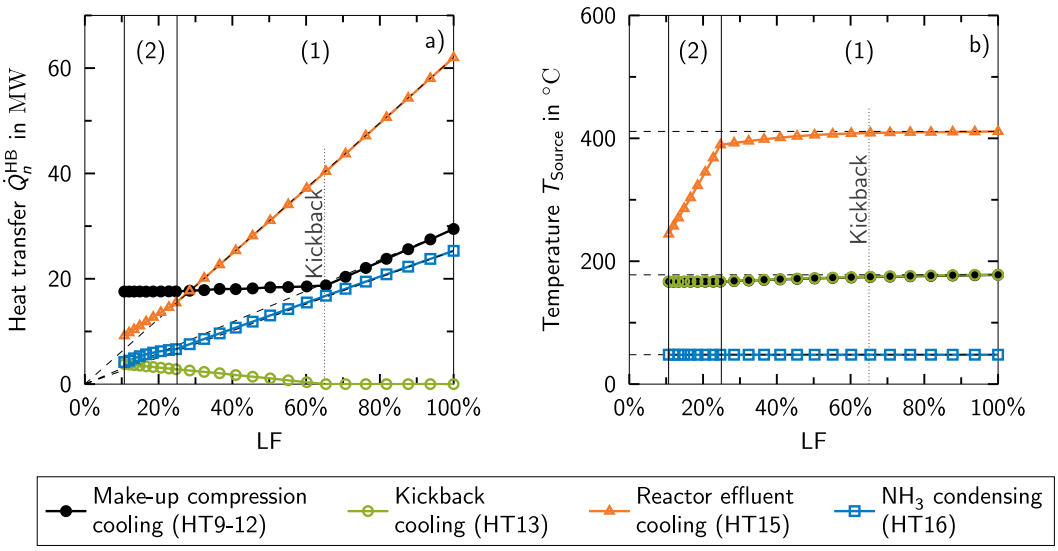

Fig. 5. (a) Amount and (b) temperature level of available heat in the HB process. Dashed lines indicate linear behavior. (1) Reducing material stream, (2) Reducing intercooling.

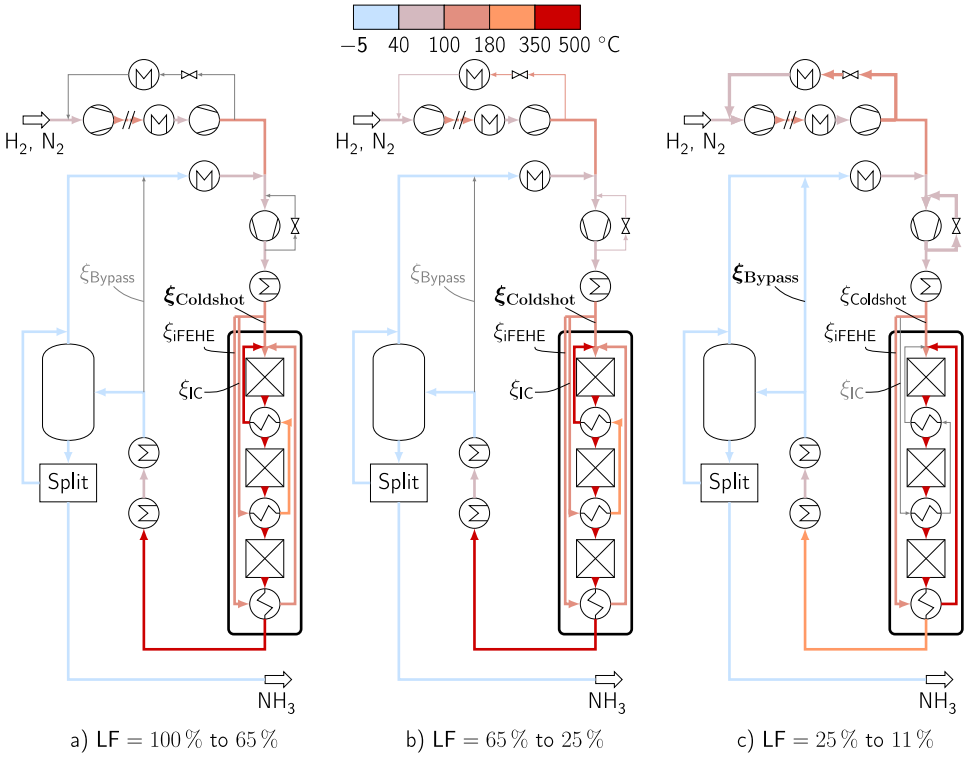

Fig. 6. Process flow diagrams of synthesis gas compression and HB loop for different part-load ranges. (For interpretation of the references to color in this figure legend, the reader is referred to the web version of this article.)
Source: Reactor sketch adopted from [46].

process. This is reflected in an increasing efficiency of the integrated SOEC, as shown in Fig. 8. At lower loads, the waste heat from the compressor, although available at a sufficiently high temperature level for steam generation, is in excess and cannot be used to further increase efficiency within the considered system boundaries. It is dissipated by the cooling tower. This excess heat at low loads is also the reason why the reduction in reactor effluent temperature in stage (2) of the partial load strategy (see Fig. 5) does not have a negative effect on the overall heat integration potential. The electric heater is merely used for the final overheating of the steam to operating temperature and for O_2 reheating. The hyperbolic increase in specific energy consumption is no longer cushioned by heat integration, but fully mirrored in the total power demand. In the overall system, this results in a dramatic drop in PtA efficiency to below 50% at minimum load, see Fig. 8.

3.2.3. Discussion of the reported outcomes

The assumption that the heat loss of the SOEC is 1% of its power demand at full load is a simplification. For future large-scale SOEC plants, this value will heavily depend on their detailed design and implementation. Key factors, among many others, are likely to include the geometry of the stacks, their arrangement to other high-temperature components, the piping, the surface-to-volume ratio, and the type and design of the insulation. However, the qualitative behavior of the heat

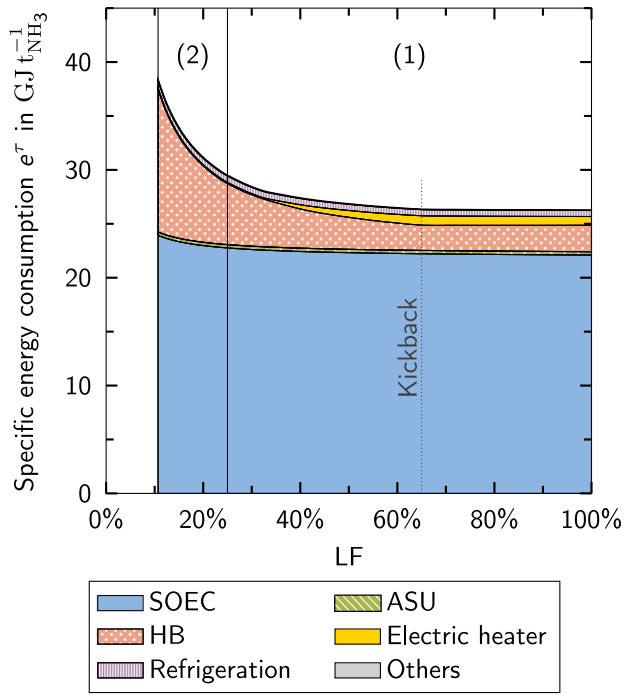

Fig. 7. Specific energy consumption of the overall system as a function of the load factor. The specific consumption of make-up compressors and SOEC heat losses increase hyperbolically with decreasing load. (1) Reducing material stream, (2) Reducing intercooling.

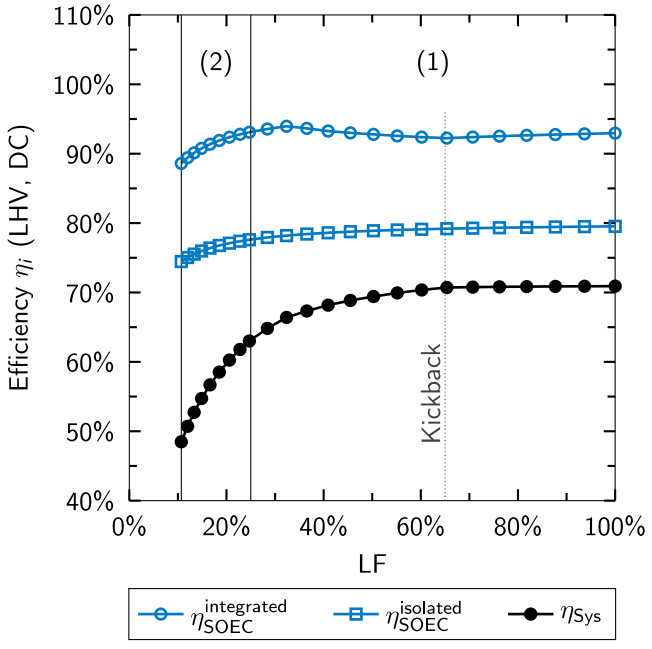

Fig. 8. Efficiencies of the SOEC (integrated, isolated) and the overall system. Losses are particularly significant at low loads. (1) Reducing material stream, (2) Reducing intercooling.

loss in part-load can be supported by considerations based on conventional models for possible heat losses by radiation (Stefan–Boltzmann's law) in Eq. (25), and convection (Newton's law of cooling) in Eq. (26).

$$\dot{Q}_{rad} = \epsilon\sigma A(T^4 - T_{env}^4) \tag{25}$$

$$\dot{Q}_{conv} = U A(T - T_{env}) \tag{26}$$

Since the system operates under thermoneutral conditions, non-recoverable heat losses can be assumed to be primarily driven by heat exchange with the environment. From Eqs. (25) and (26), it follows that heat loss is proportional to the surface area A and the temperature T. Furthermore, assuming that switched-off stacks in hot standby operation must be kept at constant temperature T through strategies that approximately preserve the flow pattern (e.g. recirculating a mixture of nitrogen and hydrogen [25]), the overall heat transfer coefficient U remains approximately unchanged. Since the surface area A is also fixed, the total heat loss remains largely unaffected by variations in load. These considerations indicate that heat losses play a significant role in modular SOEC systems and should be considered in system analyses. Ultimately, the standby strategy must be considered in the context of an operating strategy, e.g. with regard to different temperature levels of each stack in hot standby [25] and the maximum economic duration until cold standby [26].

The assumption of linear behavior of the BoP components in the SOEC system was made to focus on identifying process integration potentials with the HB process in an idealized scenario. However, it will not be valid when considering a practical implementation of the system. This may, for example, depend on the operating strategy to enable hot standby for switched-off stacks. For example, if the power demand of the O_2 recycle blower, as the only BoP power consumer considered in this work, must remain constant during part-load operation (e.g. in the context of an hot standby strategy to keep switched-off stacks at constant temperature), its contribution to the specific energy consumption increases from $0.03\,\mathrm{GJ}\,t_{NH_3}^{-1}$ at full load to $0.29\,\mathrm{GJ}\,t_{NH_3}^{-1}$ at minimum load. Although this is a notable increase, it remains less significant than the specific energy consumption of the make-up compressors in the HB process, which reach $13.2\,\mathrm{GJ}\,t_{NH_3}^{-1}$ at minimum load. However, other components may have greater limitations. For example, the flexibility of the steam boiler could be a critical factor, as its capability of load adaption directly limits the overall integration possibilities between the HB process and the SOEC system. Given this complexity, any non-ideal behavior would require further assumptions, so an idealized representation was considered a reasonable first approach to focus on fundamental integration aspects. For studies aiming at a more practical implementation, however, the part load behavior of the BoP components should also be taken into account, as these not only influence the behavior of the entire SOEC system [25], but are already increasingly becoming system-limiting components [21].

The part-load performance of the compressors is highly dependent on the selected compressor type and the employed capacity control method. Many aspects need to be taken into account when deciding on a compressor type, such as the capacity of the individual machine, the required discharge pressure, the operating range, capital cost, reliability, maintenance, the molecular weight of the gas to be compressed, space requirements, and lubrication (contamination) [71,72]. The available capacity control methods in turn depend on the compressor type and differ, for example, in terms of efficiency, complexity, and flexibility [52,71]. In conventional large-scale ammonia plants, multistage centrifugal compressors are practically the rule, mainly due to the high capacity of the individual machines (favorable for economies of scale) and their excellent reliability [8]. To align with industrial practice at the considered ammonia production scale (1356 TPD), these compressor types are selected in the study. At fixed speed, they can achieve a minimum load of approx. 75% without kickback [8]. With variable speed and other measures such as adjustable inlet guide vanes, this value can be decreased to below 50% [71]. The value of 65% of Sadlowski and van Beek [51] adopted in this paper is therefore likely to be a conservative estimate for future greenfield plants focusing on load-flexible design. However, it might not be unrealistic regarding revamps of existing large-scale plants and equipment. Nevertheless, the results in Fig. 7 demonstrate that the total specific energy demand of the PtA system is strongly related to the part-load behavior of the make-up compressors of the HB process. Therefore, in future work,

it is crucial to rigorously consider their part-load behavior. This can be done, for instance, through performance maps and control schemes in dynamic simulations. In fact, Fahr et al. [73] recently reported similar findings from a dynamic simulation of a load-flexible HB process that employed a comparable part-load strategy for both the reactor and the compressors. Their detailed compressor simulation, based on performance maps, yielded results similar to the assumption in this work: power consumption decreased linearly with load until reaching the lower operating pressure limit, after which it remained constant due to fixed pressure ratios and the maintenance of volumetric flow by kickback operation.

The adopted strategy of Fahr et al. [46] for controlled moderate pressure reduction in the loop, and its extension using the capacity control method of kickback recycling in this work is in line with patents by the companies Topsøe [12] and Casale [15]. They propose the use of the anti-surge valve of the recycle compressor, or a bypass around the reactor, respectively, for loop pressure control. Topsøe's patent further indicates that this also results in kickback operation of the make-up gas compressor [12], as assumed in this paper. Concerning the flexibility of large-scale ammonia plants, there is thus a strong incentive to reduce the kickback limit of the centrifugal make-up compressors to improve their off-design efficiency, e.g. by part-load optimized equipment design. The synergistic effect of heat integration between compressor waste heat and the SOEC system at the beginning of kickback operation would thus be shifted to lower loads and make operation in this load range significantly more attractive. Another method for expanding the load range is compressor parallelization, as suggested by Mucci et al. [74] in a Power-to-MeOH study. However, this approach requires additional effort for load sharing control and leads to higher investment costs, as it is less possible to benefit from economies of scale.

Reciprocating compressors feature significantly greater flexibility owing to additional capacity control methods such as clearance pockets and cylinder end deactivation [71]. However, they are typically used in small-scale systems, since centrifugal compressors cannot be designed for arbitrarily small volumetric flows due to manufacture limitations [8]. For example, Schulte Beerbühl et al. [75] present a process concept for a small-scale HB process operated at 400 bar and emphasize the replacement of multi-stage centrifugal compressors with reciprocating compressors. In large-scale systems like the one considered in this study, however, reciprocating compressors are disadvantaged by higher space requirements, lower reliability and higher maintenance costs due to the greater number of moving parts [71].

Given the assumption of a constant specific energy consumption for the ASU, i.e. linear part-load behavior (see Section 2.1.3), its contribution in Fig. 7 remains unchanged. Its energy requirement is dominated by the compression of air [56]. If the same capacity control method as selected for the make-up gas compressors (see Section 2.1.2) is assumed for the ASU, the specific energy consumption of the ASU would rise from $0.3\,\mathrm{GJ\,t_{NH_3}^{-1}}$ at LF = 65 % hyperbolically to $1.5\,\mathrm{GJ\,t_{NH_3}^{-1}}$ at minimum load. However, due to the non-linear part-load behavior of ASUs with respect to gas purity and their complex internal process integration [57], a more detailed analysis of the impact of their load-flexible operation on the overall system is considered beyond the scope of this work.

The optimization methodology presented in this paper assumes that the three main technologies (SOEC system, ASU, and HB process) operate at the same part-load state owing to the mass balance constraint in Eq. (16). In reality, this will rarely be the case due to differences in flexibility and load ramping of the technologies. If the electricity supply is intermittent, these differences can also be compensated for by intermediate storage or oversizing, for example, to meet an annual production target. Furthermore, the optimal heat integration of each load step resulting from this work, even if the technical feasibility in principle is ensured by the pinch analysis, can be a challenge in practice when it comes to finding a single design that achieves the theoretical minimum energy requirement in each load condition. This is due to the fact that a permanent pairing of hot and cold streams has to be defined when implementing the system. Strictly speaking, part-load operation would also have to be taken into account in the design of heat exchangers used for heat integration, for example in terms of flow-dependent pressure losses and heat transfer coefficients. The system integration is, however, likely easier at lower loads, as there is more heat to pass around. A more practical approach for real-world implementation, would be to develop a robust heat integration scheme that delivers a near-optimal performance over the entire operating range. This could involve, for example, incorporating additional or oversized heat exchangers compared to a full-load design to accommodate load fluctuations, as demonstrated in [46] for the scope of heat integration within the ammonia reactor. Such a design would inherently involve trade-offs between proximity to the minimum energy requirement identified in this work and the associated investment required to achieve it, as similarly shown in [18] for the ammonia reactor. While this study does not aim to propose a detailed system design, it provides insights into the potential synergies between the SOEC system and the Haber–Bosch process. This particularly includes the influence of the selected part-load strategies, the behavior of which can have a significant impact on the potential for heat integration. By linking the non-linear behavior of heat flows and temperatures in the HB process to the method of heat integration, this work reveals key factors that would need to be considered when transitioning from theoretical optimization to practical implementation.

4. Summary and outlook

In this work, we presented an SOEC-coupled HB process and investigated its heat integration potentials depending on specific part-load strategies through optimization. A model of a low-pressure SOEC system was extended with a load-independent heat loss to reflect the cost of a modular part-load strategy in which individual stacks can be switched to hot standby. Based on a rating model of a large-scale, load-flexible ammonia reactor, a two-stage part-load trajectory with simplified temperature control was determined. This trajectory, in the load range of 10.7% to 100%, was used to capture the non-linearities in heat flows and temperatures. To avoid compressor surge, kickback operation was considered below a minimum volumetric flow as the capacity control method for the centrifugal recycle and make-up compressors. The load range of the HB process was discretized, each section linearized, and the heat integration with the other technologies was solved as a linear programming problem.

During full load operation, heat integration with the HB process led to an increase in the efficiency (LHV, DC) of the SOEC system from 70.5% to 93.0%. This was primarily due to the use of the reaction heat and compressor waste heat for steam generation. The resulting overall specific energy consumption of $26.4\,\mathrm{GJ\,t_{NH_3}^{-1}}$ and an efficiency of 70.9% (LHV, DC) are significantly lower than processes based on low-temperature electrolysis and comparable to current state-of-the-art SMR-based processes. However, there still remained a gap of $0.8\,\mathrm{GJ\,t_{NH_3}^{-1}}$ in the heat demand of the SOEC, which needed to be covered by other heat sources, e.g. an electrical heater.

In part load, the specific energy consumption of the system remained nearly constant down to 65% part load. Below, the make-up gas compressor switched to kickback operation, i.e. a part of the compressed discharge gas is recycled back to the suction side to avoid compressor surge. This capacity control method led to a significant increase in specific energy consumption. Moreover, internal recycling resulted in a corresponding production of waste heat, which had to be removed in the intercoolers between compression stages. However, this excess waste heat, available at a temperature suitable for low-pressure steam generation, could increasingly replace the costly electrical heater as heat source for steam production. At a load of 100%, 14.3% of the steam generation heat demand (or $0.7\,\mathrm{GJ\,t_{NH_3}^{-1}}$) had to be supplied by electrical heating, a requirement that remained nearly constant

down to a load of 65%. As the load decreased further, the need for electrical heating gradually diminished, reaching 0% at 32.4% load. This created a synergy in the medium load range, mitigating the increase of specific energy consumption caused by compressor kickback. At a load of 32.4%, all the heat required for steam production was sourced from the ammonia reactor effluent and the waste heat from the compressors. The role of the electrical heater was reduced to only the final heating of inlet streams for the SOEC stacks. Towards lower loads, the hyperbolic increase in both, specific compressor consumption and SOEC heat loss, became increasingly dominant. At the minimum load of 10.7%, this culminated in an increase of 46% in overall specific energy consumption compared to full load, causing the overall efficiency to fall below 50% (LHV, DC). Of this increase in specific energy consumption, approximately 6% was attributable to SOEC heat loss and approximately 40% to the make-up gas compressor.

The results demonstrate the critical impact that part-load strategies of the individual technologies have on the part-load performance of the overall system and underscore the importance of not neglecting them in multi-period system analyses. For the SOEC, the findings emphasize the minimization of heat losses in the design of modular SOEC systems, especially when considering hot standby operation. For the HB process, it was shown that the make-up gas compressor, along with its capacity control method, not only impacts the overall system in terms of its direct energy consumption, but also plays a crucial rule in heat integration decisions in process design.

It may be that the non-linear part-load behavior of the other technologies neglected in this study, e.g. the BoP components of the SOEC, the ASU, and the refrigeration unit, can also influence the overall system. Therefore, they should be taken into account in future work. Furthermore, dynamic assessments of load changes and control concepts are essential in flexibility studies to determine realistic load ramps and should include the make-up gas and recycle compressors in particular. In conjunction with detailed cost estimates and storage concepts, these considerations will allow a thorough and realistic multi-period evaluation of the entire Power-to-Ammonia system.

Abbreviations

ASU	Air separation unit
BoP	Balance of plant
CT	Cooling tower
DC	Direct current
EH	Electric heater
FEHE	Feed-effluent heat exchanger
HB	Haber-Bosch
HT	Heat transfer
IC	Intercooler
LHV	Lower heating value
PtA	Power-to-Ammonia
RU	Refrigeration unit
SB	Steam boiler
SOEC	Solid oxide electrolysis cell
TPD	Tons per day

Nomenclature

A	Area	m^2
a	Model parameter	–
B_Ω	Material constant	$S\,K\,m^{-2}$
b	Model parameter	–
e	Specific energy consumption	$GJ\,t_{NH_3}^{-1}$
E_A	Activation energy	$kJ\,mol^{-1}$
E_{act}	Activation energy	$J\,mol^{-1}$
f	Fugacity	bar
F	Faraday constant	$A\,s\,mol^{-1}$
$\Delta\bar{G}_R^0$	Standard molar Gibbs free energy of reaction	$kJ\,mol^{-1}$
j	Current density	$A\,cm^{-2}$
j_0	Exchange current density	$A\,cm^{-2}$
k_0	Pre-exponential factor	$kmol\,bar^{0.5}\,h^{-1}\,m_{cat}^3$
K_f	Equilibrium constant	–
LF	Load factor	–
$\dot{M}$	Mass flow	$kg\,s^{-1}$
m	Model parameter	–
P_{el}	Electrical power	kW
p	Pressure	bar
p_i	Partial pressure of component i	bar
p^0	Reference pressure	bar
$\dot{Q}$	Heat flow/transfer	kW
r	Reaction rate	$kmol\,m_{cat}^{-3}\,h$
R	Residual heat	kW
$\bar{R}$	Ideal gas constant	$J\,mol^{-1}\,K$
R_Ω	Ohmic resistance	Ω
T	Temperature	°C, K
U	Overall heat transfer coefficient	$W\,m^{-2}\,K$
V_{op}	Operating voltage	V
V	Volume	m^3
y_i	Molar fraction of component i	–
z	Number of transferred electrons	–
α	Transfer coefficient	–
γ	Pre-factor	$A\,K^{-1}\,m^2$
γ^τ	Size factor of technology τ	–
η	Efficiency	–
η_{act}	Activation overpotential	V
ν	Stoichiometric coefficient	–
ξ	Split factor	–
Π	Compression ratio	–

CRediT authorship contribution statement

Matthias Schiedeck: Writing – review & editing, Writing – original draft, Methodology, Investigation, Conceptualization. **Rafael Nogueira Nakashima:** Writing – review & editing, Supervision, Methodology, Conceptualization. **Henrik Lund Frandsen:** Writing – review & editing, Supervision, Conceptualization.

Declaration of Generative AI and AI-assisted technologies in the writing process

During the preparation of this work the authors used GPT-4o from OpenAI in order to improve the quality of writing in terms of grammatical correctness and stylistics. After using this tool/service, the authors reviewed and edited the content as needed and take full responsibility for the content of the published article.

Declaration of competing interest

The authors declare the following financial interests/personal relationships which may be considered as potential competing interests: Henrik Lund Frandsen reports financial support was provided by Innovationsfonden. If there are other authors, they declare that they have no known competing financial interests or personal relationships that could have appeared to influence the work reported in this paper.

Acknowledgments

This contribution is part of the COMPAS project funded by the Innovation Fund Denmark – 1150-00001B. Further information is available at https://missiongreenfuels.dk/. Innovation Fund Denmark

Appendix A. Supplementary data

Supplementary material related to this article can be found online at https://doi.org/10.1016/j.ijhydene.2025.02.335.

Data availability

No data was used for the research described in the article. The energy integration optimization framework Vivi (Nakashima 2022) is available at https://github.com/srnogueira/vivi.

References

[1] Rouwenhorst KH. Ammonia, 4. Green ammonia production. In: Ullmann's encyclopedia of industrial chemistry. Wiley-VCH Verlag GmbH & Co. KGaA; 2020, http://dx.doi.org/10.1002/14356007.w02_w02.
[2] Royal Society (Great Britain). Ammonia: zero-carbon fertiliser, fuel and energy store: policy briefing. Royal Society; 2020.
[3] Taylor M, Al-Zoghul S, Ralon P. Renewable power generation costs in 2022. International Renewable Energy Agency (IRENA); 2023,
[4] Dechany A, Van Geem K, Proost J. Process implications of electrifying ammonia production. Curr Opin Chem Eng 2023;40:100915. http://dx.doi.org/10.1016/j.coche.2023.100915.
[5] Weikl M, Peschel A. Industrial view on hydrogen carriers for intercontinental transport. Curr Opin Green Sustain Chem 2023;100843. http://dx.doi.org/10.1016/j.cogsc.2023.100843.
[6] Rouwenhorst KH, Travis AS, Lefferts L. 1921–2021: A century of renewable ammonia synthesis. Sustain Chem 2022;3(2):149–71. http://dx.doi.org/10.3390/suschem3020011.
[7] Mucci S, Mitsos A, Bongartz D. Power-to-X processes based on PEM water electrolyzers: A review of process integration and flexible operation. Comput Chem Eng 2023;108260. http://dx.doi.org/10.1016/j.compchemeng.2023.108260.
[8] Appl M. Ammonia, 2. Production processes. In: Ullmann's encyclopedia of industrial chemistry. Wiley-VCH Verlag GmbH & Co. KGaA; 2012, http://dx.doi.org/10.1002/14356007.o02_o11.
[9] Hooper CW. Ammonia synthesis: commercial practice. In: Jennings J, editor. Catalytic ammonia synthesis: fundamentals and practice. Springer Science+Business Media New York; 1991, p. 252–83.
[10] Comission E. Reference document on best available techniques for the manufacture of large volume inorganic chemicals - ammonia, acids and fertilisers. Technical Report, European Comission; 2007, URL https://eippcb.jrc.ec.europa.eu/sites/default/files/2022-03/LVIC-AAF.pdf.
[11] Hydrogen N. Danish dynamic ammonia production is world first. 2023, URL https://nelhydrogen.com/articles/in-depth/danish-dynamic-ammonia-production-is-world-first/, [Accessed 18 October 2023].
[12] Speth CH, Hultqvist M, Han PA. Method for the control of pressure in a loop for the preparation of ammonia or methanol. 2021, URL https://patents.google.com/patent/WO2021233780A1/en?oq=WO2021233780A1.
[13] Ostuni R, Zardi F. Method for load regulation of an ammonia plant. 2013, URL https://patents.google.com/patent/CA2790545A1/en.
[14] Luyben WL. Design and control of a cooled ammonia reactor. In: Rangaiah GP, Kariwala V, editors. Plantwide control: recent developments and applications. John Wiley & Sons; 2012, p. 273–92.
[15] Rizzi M. Control of an ammonia synthesis loop at partial load. 2019, URL https://patents.google.com/patent/EP3819261A1/en.
[16] Cheema II, Krewer U. Optimisation of the autothermal NH3 production process for power-to-ammonia. Processes 2019;8(1). http://dx.doi.org/10.3390/pr8010038.
[17] Kolbe B, Roosen C, Johanning J, Schulte-Beerbühl S, Schultmann F. Method and system for producting a product gas under changing load conditions. 2017, URL https://patents.google.com/patent/WO2017153304A1/un.
[18] Fahr S, Schiedeck M, Reinke M, Bohn J-P, Rehfeldt S, Peschel A, Klein H. Simultaneous design and part-load optimization of an industrial ammonia synthesis reactor. Chem Eng J 2024;480:148302. http://dx.doi.org/10.1016/j.cej.2023.148302.
[19] Rosbo JW, Ritschel TK, Hørsholt S, Huusom JK, Jørgensen JB. Flexible operation, optimisation and stabilising control of a quench cooled ammonia reactor for power-to-ammonia. Comput Chem Eng 2023;108316. http://dx.doi.org/10.1016/j.compchemeng.2023.108316.
[20] Kong B, Zhang Q, Daoutidis P. Nonlinear model predictive control of flexible ammonia production. Control Eng Pract 2024;148:105946. http://dx.doi.org/10.1016/j.conengprac.2024.105946.
[21] Hauch A, Küngas R, Blennow P, Hansen AB, Hansen JB, Mathiesen BV, Mogensen MB. Recent advances in solid oxide cell technology for electrolysis. Science 2020;370(6513). http://dx.doi.org/10.1126/science.aba6118.
[22] Wang Y, Banerjee A, Deutschmann O. Dynamic behavior and control strategy study of CO2/H2O co-electrolysis in solid oxide electrolysis cells. J Power Sources 2019;412:255–64. http://dx.doi.org/10.1016/j.jpowsour.2018.11.047.
[23] Cai Q, Adjiman CS, Brandon NP. Optimal control strategies for hydrogen production when coupling solid oxide electrolysers with intermittent renewable energies. J Power Sources 2014;268:212–24. http://dx.doi.org/10.1016/j.jpowsour.2014.06.028.
[24] Schefold J, Brisse A, Surrey A, Walter C. 80,000 current on/off cycles in a one year long steam electrolysis test with a solid oxide cell. Int J Hydrog Energy 2020;45(8):5143–54. http://dx.doi.org/10.1016/j.ijhydene.2019.05.124.
[25] Tomberg M, Heddrich MP, Ansar SA, Friedrich KA. Operation strategies for a flexible megawatt scale electrolysis system for synthesis gas and hydrogen production with direct air capture of carbon dioxide. Sustain Energy Fuels 2023;7(2):471–84. http://dx.doi.org/10.1039/D2SE01473D.
[26] van't Noordende H, van Berkel F, Stodolny M. Next level solid oxide electrolysis. 2023, URL https://ispt.eu/media/20230508-FINAL-SOE-public-report-ISPT.pdf.
[27] Cinti G, Frattini D, Jannelli E, Desideri U, Bidini G. Coupling solid oxide electrolyser (SOE) and ammonia production plant. Appl Energy 2017;192:466–76. http://dx.doi.org/10.1016/j.apenergy.2016.09.026.
[28] Hansen JB. Power-to-ammonia for fertilizers, chemicals, and as an energy vector. In: Sitte W, Merkle R, editors. High-temperature electrolysis. IOP Publishing; 2023, http://dx.doi.org/10.1088/978-0-7503-3951-3.
[29] Zhang H, Wang L, Maréchal F, Desideri U, et al. Techno-economic comparison of green ammonia production processes. Appl Energy 2020;259:114135. http://dx.doi.org/10.1016/j.apenergy.2019.114135.
[30] Campion N, Nami H, Swisher PR, Hendriksen PV, Münster M. Techno-economic assessment of green ammonia production with different wind and solar potentials. Renew Sustain Energy Rev 2023;173:113057. http://dx.doi.org/10.1016/j.rser.2022.113057.
[31] Nami H, Hendriksen PV, Frandsen HL. Green ammonia production using current and emerging electrolysis technologies. Renew Sustain Energy Rev 2024;199:114517. http://dx.doi.org/10.1016/j.rser.2024.114517.
[32] Nakashima RN, Hendriksen PV, Frandsen HL. Optimization of energy systems sizing and operation including heat integration and storage. In: 36th international conference on efficiency, cost, optimization, simulation and environmental impact of energy systems. ECOS; 2023, p. 1375–86. http://dx.doi.org/10.52202/069564-0125.
[33] AlZahrani AA, Dincer I. Thermodynamic and electrochemical analyses of a solid oxide electrolyzer for hydrogen production. Int J Hydrog Energy 2017;42(33):21404–13. http://dx.doi.org/10.1016/j.ijhydene.2017.03.186.
[34] Petipas F, Brisse A, Bouallou C. Thermal management of solid oxide electrolysis cell systems through air flow regulation. Chem Eng Trans 2017;61:1069–74. http://dx.doi.org/10.3303/CET1761176.
[35] Nami H, Rizvandi OB, Chatzichristodoulou C, Hendriksen PV, Frandsen HL. Techno-economic analysis of current and emerging electrolysis technologies for green hydrogen production. Energy Convers Manage 2022;269:116162. http://dx.doi.org/10.1016/j.enconman.2022.116162.
[36] Nakashima RN, de Oliveira Junior S. Thermodynamic evaluation of solid oxide fuel cells converting biogas into hydrogen and electricity. Int J Thermodyn 2021;24(3):204–14. http://dx.doi.org/10.5541/ijot.877847.
[37] Nakashima RN, de Oliveira Junior S. Multi-objective optimization of biogas systems producing hydrogen and electricity with solid oxide fuel cells. Int J Hydrog Energy 2023;48(31):11806–22. http://dx.doi.org/10.1016/j.ijhydene.2021.08.195.
[38] Nakashima RN, Nami H, Nemati A, Butera G, Vang P, Hendriksen SdJ, Frandsen HL. Integration of electrolysis with pyrolysis: effects of carbon conversion in methanol production. In: 7th international conference on contemporary problems of thermal engineering. 2022.
[39] Bao C, Jiang Z, Zhang X. Modeling mass transfer in solid oxide fuel cell anode: I. Comparison between fickian, stefan-maxwell and dusty-gas models. J Power Sources 2016;310:32–40. http://dx.doi.org/10.1016/j.jpowsour.2016.01.099.
[40] Posdziech O, Schwarze K, Brabandt J. Efficient hydrogen production for industry and electricity storage via high-temperature electrolysis. Int J Hydrog Energy 2019;44(35):19089–101. http://dx.doi.org/10.1016/j.ijhydene.2018.05.169.
[41] Liu H, Høgh J, Blennow P, Sun X, Zong Y, Chen M. Assessing fluctuating wind to hydrogen production via long-term testing of solid oxide electrolysis stacks. Appl Energy 2024;361:122938. http://dx.doi.org/10.1016/j.apenergy.2024.122938.
[42] Lange H, Klose A, Lippmann W, Urbas L. Technical evaluation of the flexibility of water electrolysis systems to increase energy flexibility: A review. Int J Hydrog Energy 2023. http://dx.doi.org/10.1016/j.ijhydene.2023.01.044.
[43] Buttler A, Spliethoff H. Current status of water electrolysis for energy storage, grid balancing and sector coupling via power-to-gas and power-to-liquids: A review. Renew Sustain Energy Rev 2018;82:2440–54. http://dx.doi.org/10.1016/j.rser.2017.09.003.

[44] Mathiesen BV, Ridjan I, Connolly D, Nielsen MP, Hendriksen PV, Mogensen MB, Jensen SH, Ebbesen SD. Technology data for high temperature solid oxide electrolyser cells, alkali and PEM electrolysers. Department of development and planning, Aalborg University; 2013.
[45] Kruse N, Tiedemann W, Hoven I, Deja R, Peters R, Blum L, Peters R. Experimental investigation of efficiency maximization in solid oxide electrolysis systems by internal steam and heat recovery. ECS Trans 2021;103(1):555. http://dx.doi.org/10.1149/10301.0555ecst.
[46] Fahr S, Schiedeck M, Schwarzhuber J, Rehfeldt S, Peschel A, Klein H. Design and thermodynamic analysis of a large-scale ammonia reactor for increased load flexibility. Chem Eng J 2023;471:144612. http://dx.doi.org/10.1016/j.cej.2023.144612.
[47] Rossetti I. Reactor design, modelling and process intensification for ammonia synthesis. In: Inamuddin, Boddula R, Asiri AM, editors. Sustainble ammonia production. Springer; 2020, p. 17–48. http://dx.doi.org/10.1007/978-3-030-35106-9_2.
[48] Gillespie LJ, Beattie JA. The thermodynamic treatment of chemical equilibria in systems composed of real gases. I. An approximate equation for the mass action function applied to the existing data on the haber equilibrium. Phys Rev 1930;36(4):743. http://dx.doi.org/10.1103/PhysRev.36.743.
[49] Dyson D, Simon J. Kinetic expression with diffusion correction for ammonia synthesis on industrial catalyst. Ind Eng Chem Fundam 1968;7(4):605–10. http://dx.doi.org/10.1021/i160028a013.
[50] Wang L, Chen M, Küngas R, Lin T-E, Diethelm S, Maréchal F, et al. Power-to-fuels via solid-oxide electrolyzer: Operating window and techno-economics. Renew Sustain Energy Rev 2019;110:174–87. http://dx.doi.org/10.1016/j.rser.2019.04.071.
[51] Sadlowski M, van Beek M. Ecologic potential for flexible methanol production from steel mill off-gases. Chem Ing Tech 2020;92(10):1416–24. http://dx.doi.org/10.1002/cite.202000085.
[52] Lüdtke KH. Process centrifugal compressors. Springer Berlin, Heidelberg; 2004, http://dx.doi.org/10.1007/978-3-662-09449-5.
[53] Böcker N, Grahl M, Tota A, Häussinger P, Leitgeb P, Schmücker B. Nitrogen. In: Ullmann's encyclopedia of industrial chemistry. Wiley-VCH Verlag GmbH & Co. KGaA; 2013, http://dx.doi.org/10.1002/14356007.a17_457.pub2.
[54] Kender R, Wunderlich B, Thomas I, Peschel A, Rehfeldt S, Klein H. Pressure-driven dynamic simulation of start up and shutdown procedures of distillation columns in air separation units. Chem Eng Res Des 2019;147:98–112. http://dx.doi.org/10.1016/j.cherd.2019.04.031.
[55] Haider P, Freko P, Lochner S, Reiter T, Rehfeldt S, Klein H. Design of a test rig for the simulation of startup procedures in main heat exchangers of air separation plants. Chem Eng Res Des 2019;147:90–7. http://dx.doi.org/10.1016/j.cherd.2019.04.025.
[56] Mitsos A, Schäfer P, Caspari A, Ecker A, Frank R, Freko P, Haider P, Kender R, King R, Klein H, Lange A, Lochner S, Mhamdi A, Niehuis R, Obermeier A, Peschel A, Rehfeldt S, Schieblitz F, Thomas I, Windmeier C, Wunderlich B. C.4 luftzerlegung. In: Sauer A, Abele E, Buhl HU, editors. Energieflexibilität in der deutschen Industrie. Fraunhofer Verlag; 2019, URL https://synergie-projekt.de/wp-content/uploads/2020/08/urn_nbn_de_0011-n-5659211.pdf.
[57] Cao Y, Swartz CL, Flores-Cerrillo J. Optimal dynamic operation of a high-purity air separation plant under varying market conditions. Ind Eng Chem Res 2016;55(37):9956–70. http://dx.doi.org/10.1021/acs.iecr.6b02090.
[58] Leiva C, Poblete D, Aguilera T, Acuña C, Quintero F. Air separation units (ASUs) simulation using aspen hysys at oxinor I of air liquid Chile SA plant. Pol J Chem Technol 2020;22(1):10–7. http://dx.doi.org/10.2478/pjct-2020-0003.
[59] Gürsoy E, Gedik E, Georgiev AG, Keçebaş A, Kurt H. Performance improvement of air separation unit for an iron-steel industry using enhanced exergy analysis. J Therm Anal Calorim 2024;149(8):3267–84. http://dx.doi.org/10.1007/s10973-024-12921-2.
[60] Moshfeghian M. Refrigeration with flash economizer vs. Simple refrigeration system. 2008, URL http://www.jmcampbell.com/tip-of-the-month/2008/01/refrigeration-with-flash-economizer-vs-simple-refrigeration-system/.
[61] Turton R, Bailie RC, Whiting WB, Shaeiwitz JA. Analysis, synthesis and design of chemical processes. fourth ed.. Pearson Education; 2012, http://dx.doi.org/10.1016/j.energy.2018.03.166,
[62] Marechal F, Kalitventzeff B. Targeting the minimum cost of energy requirements: a new graphical technique for evaluating the integration of utility systems. Comput Chem Eng 1996;20:S225–30. http://dx.doi.org/10.1016/0098-1354(96)00048-8.
[63] Nakashima RN. Modelling, simulation and optimization of biogas conversion routes integrated with fuel cell technology. (Ph.D. thesis), São Paulo: Universidade de São Paulo; 2022, http://dx.doi.org/10.11606/T.3.2022.tde-26082022-081436, URL https://www.teses.usp.br/teses/disponiveis/3/3150/tde-26082022-081436/.
[64] Papoulias SA, Grossmann IE. A structural optimization approach in process synthesis—II: Heat recovery networks. Comput Chem Eng 1983;7(6):707–21. http://dx.doi.org/10.1016/0098-1354(83)85023-6.
[65] Hansen JB, Hendriksen PV. The SOC4NH3 Project. Production and use of ammonia by solid oxide cells. ECS Trans 2019;91(1):2455. http://dx.doi.org/10.1149/09101.2455ecst.
[66] Molla TT, Kwok K, Frandsen HL. Modeling the mechanical integrity of generic solid oxide cell stack designs exposed to long-term operation. Fuel Cells 2019;19(1):96–109. http://dx.doi.org/10.1002/fuce.201800081.
[67] Wang L, Pérez-Fortes M, Madi H, Diethelm S, Maréchal F, et al. Optimal design of solid-oxide electrolyzer based power-to-methane systems: A comprehensive comparison between steam electrolysis and co-electrolysis. Appl Energy 2018;211:1060–79. http://dx.doi.org/10.1016/j.apenergy.2017.11.050.
[68] Beyrami J, Nakashima RN, Nemati A, Frandsen HL. Lifetime and performance of solid oxide electrolysis stacks and systems under different operation modes and conditions. Int J Hydrog Energy 2025;102:980–95. http://dx.doi.org/10.1016/j.ijhydene.2025.01.028.
[69] Hansen JB. Solid oxide electrolysis–a key enabling technology for sustainable energy scenarios. Faraday Discuss 2015;182:9–48. http://dx.doi.org/10.1039/C5FD90071A.
[70] Beyrami J, Nakashima RN, Nemati A, Frandsen HL. Degradation modeling in solid oxide electrolysis systems: A comparative analysis of operation modes. Energy Convers Manage: X 2024;100653. http://dx.doi.org/10.1016/j.ecmx.2024.100653.
[71] Gallick P, Phillippi G, Williams BF, et al. What's correct for my application-a centrifugal or reciprocating compressor? In: Proceedings of the 35th turbomachinery symposium. Texas A&M University. Turbomachinery Laboratories; 2006.
[72] Peschel A. Industrial perspective on hydrogen purification, compression, storage, and distribution. Fuel Cells 2020;20(4):385–93. http://dx.doi.org/10.1002/fuce.201900235.
[73] Fahr S, Kender R, Bohn J-P, Rehfeldt S, Peschel A, Klein H. Dynamic simulation of a highly load-flexible haber–bosch plant. Int J Hydrog Energy 2025;102:1231–42. http://dx.doi.org/10.1016/j.ijhydene.2025.01.039.
[74] Mucci S, Mitsos A, Bongartz D. Cost-optimal power-to-methanol: Flexible operation or intermediate storage? J Energy Storage 2023;72:108614. http://dx.doi.org/10.1016/j.est.2023.108614.
[75] Schulte Beerbühl S, Kolbe B, Roosen C, Schultmann F. Ammoniaksynthese als Beispiel einer stofflichen Nutzung von intermittierend erzeugtem wasserstoff. Chem Ing Tech 2014;5(86):649–57. http://dx.doi.org/10.1002/cite.201300167.